

Review

A Review of Cooling Studies on Gas Turbine Rotor Blades with Rotation

Shyy Woei Chang ^{1,*} , Pey-Shey Wu ² , Ting-Yu Wan ¹ and Wei-Ling Cai ¹¹ Department of Systems and Naval Mechatronic Engineering, National Cheng Kung University, No. 1, University Road, Tainan City 70101, Taiwan² Department of Mechanical and Automation Engineering, Da-Yeh University, No. 168, University Road, Dacun, Changsha 51591, Taiwan

* Correspondence: swchang@mail.ncku.edu.tw

Abstract: Increases in power density and thermal efficiency of a highly efficient gas turbine engine motivate an ever-mounting turbine entry temperature. The combined metallurgical and cooling advancements ensure the structural integrity of a gas turbine rotor blade that spins at high rotor speeds in a gas stream with temperatures above the melting point of the blade material. The cooling performances promoted by a variety of heat transfer enhancement methods typical of the coolant channels of the leading edge, the mid-chord region, and the trailing edge of a gas turbine rotor blade are reviewed. The manifested rotational effects on the aerothermal performances of impinging jets and swirl chambers for leading-edge cooling, multi-pass ribbed, dimpled, and/or wavy channels over the mid-chord region, as well as pin fin and latticework narrow ducts in the trailing edge of a gas turbine rotor blade, are summarized and cross-examined. Research orientations for future cooling studies aimed at preventing the development of hot spots in a gas turbine rotor blade are recommended.

Keywords: gas turbine rotor blade; internal cooling; rib; dimple; impingement; swirl chamber; latticework



Citation: Chang, S.W.; Wu, P.-S.; Wan, T.-Y.; Cai, W.-L. A Review of Cooling Studies on Gas Turbine Rotor Blades with Rotation. *Inventions* **2023**, *8*, 21. <https://doi.org/10.3390/inventions8010021>

Academic Editor: Ping-Hei Chen

Received: 14 November 2022

Revised: 12 December 2022

Accepted: 4 January 2023

Published: 12 January 2023



Copyright: © 2023 by the authors. Licensee MDPI, Basel, Switzerland. This article is an open access article distributed under the terms and conditions of the Creative Commons Attribution (CC BY) license (<https://creativecommons.org/licenses/by/4.0/>).

1. Internal Cooling of a Gas Turbine Rotor Blade

The increase in the thermodynamic efficiency of a gas turbine engine at a specific propulsive efficiency is permissible by raising the overall pressure ratio. In this respect, an optimal turbine entry temperature (TET) corresponds to an overall pressure ratio. Yet, an increase in TET at a specific engine thrust enables a further increase in the engine bypass ratio and reduces engine weight, which upraises the engine power-to-weight ratio. However, the limitation of TET is set by the maximum sustainable material temperature of the high-pressure turbine rotor blades. Over the last five decades, the mild TET increase of approximately three K/year has been achieved through the progresses in turbine material technology. A substantial TET increase of approximately 10 K/year is associated with the advancements in its cooling effectiveness. However, an increase in the cooling flow rate in a gas turbine blade to permit further TET elevation is imperfect, as the coolant consumption also accounts for engine losses which attributes to overall engine efficiency deficits. The major cause of such TET increases are the novel heat transfer enhancement (HTE) methods invented to improve the performance of an integrated cooling scheme for a gas turbine rotor blade.

In a gas turbine rotor blade, the coolant flow is often channeled in radially outward or inward directions. Instead of arranging these radial coolant channels in parallel, the coolant channels are interconnected by sharp bends in a serpentine manner to reduce coolant consumption. Local surface heat transfer enhancement devices, such as ribs and pin fins, are mounted on the leading and trailing endwalls. In particular, the configuration of a multi-pass cooling network must comply with the blade profile with varying shape and flow directions. The pressurized airflow through the internal coolant channel also

facilitates film and transpiration cooling over the outer surface of a gas turbine blade. The mutually affected internal and external cooling flows work together to provide efficient cooling in numerical applications.

In addition to the complicated coolant channel geometries, the coolant flow is constrained in the rotating channels at a speed in the range of 5000–20,000 rev/min to give rise to Coriolis and centrifugal forces that alter the flow structures, and hence cooling performances, from non-rotating conditions. With a radial outflow (inflow), the Coriolis forces on the plane perpendicular to the channel axis act toward the trailing (leading) channel wall, inducing Coriolis secondary flows to generate peripheral heat transfer variation. Meanwhile, a rich mode of vortical flows are induced by ribs or pin fins to interact with Coriolis secondary flows which modify the local heat transfer rate. With such complex vortical interactions, the local minimum heat transfer location at which the hot fluids are confluent or trapped exhibits the impaired cooling effectiveness from that of a non-rotating channel to raise the hot spot temperature. Moreover, buoyancy interactions (due to the temperature-dependent coolant density variation in a strong centrifugal force field) tend to motivate the warmer fluid toward the center of rotation. The physical manifestations of rotation, namely the Coriolis and rotating buoyancy forces, also affect the turbulent activities in a rotating channel.

The combined effects of rotation, HTE devices, and channel geometries on the cooling performance of a rotating channel have been studied extensively in recent years. Following a strategic goal aimed at generating the heat transfer results in realistic engine conditions, the research progress from comprehending the fundamental principles via the theoretical and experimental studies of simplified models at weak rotational manifestations is evolving toward the experimental and numerical studies with realistic channel configurations in the scenarios close to engine conditions. Based on the dynamic similarity law, the realistic engine conditions of a coolant flow in a rotating channel are specified. The laboratory strategies developed for emulating the engine conditions at a reduced rotor speed are described as follows.

2. Strategy for Engine Condition Emulation

As illustrated previously, the cooling performance inside a gas turbine rotor blade is affected by rotation as well as the complexities introduced by the HTE method and the geometry of the coolant passages. The fundamental features of the rotationally induced body forces include the well-known Coriolis and centrifugal forces with the third component of inertial force arising from any rate of angular velocity change during an acceleration or deceleration period of the engine. The dimensionless groups characterizing the rotational influences on flow and heat transfer performances of a channel that rotates orthogonally in the flow direction are identified from the governing flow equations. The experimental strategy aimed at emulating the engine conditions for the coolant flows inside a gas turbine rotor is often developed to match the realistic ranges of these dimensionless flow parameters.

The derivation of these dimensionless flow equations begins with a description of the way in which a fluid motion referred to a rotating frame of reference must be adapted to account for the fact that Newton's motion law is applicable to an inertial frame of reference. Figure 1a depicts a segmental flow passage of an arbitrary cross-section that rotates and translates with respect to a convenient inertial reference frame $O'X'Y'Z'$. Relative to the inertial $O'X'Y'Z'$ frame, the selected origin $oxyz$, which is synchronous with the rotating/translating motions of the moving duct, is translating with velocity \vec{v}_0 , acceleration \vec{f}_0 , and rotating with an angular velocity $\vec{\omega}$. The acceleration (\vec{f}) of a fluid particle, P, with a position vector, \vec{r}_a , relative to the moving frame $oxyz$ at any time, t , that has a velocity, \vec{v} , is defined by Equation (1) [1].

$$\vec{f} = \frac{\partial^2 \vec{a}}{\partial t^2} + \frac{\partial \vec{\omega}}{\partial t} \times \vec{a} + 2\vec{\omega} \times \frac{\partial \vec{a}}{\partial t} + \vec{\omega} \times (\vec{\omega} \times \vec{a}) + \vec{f}_0 \quad (1)$$

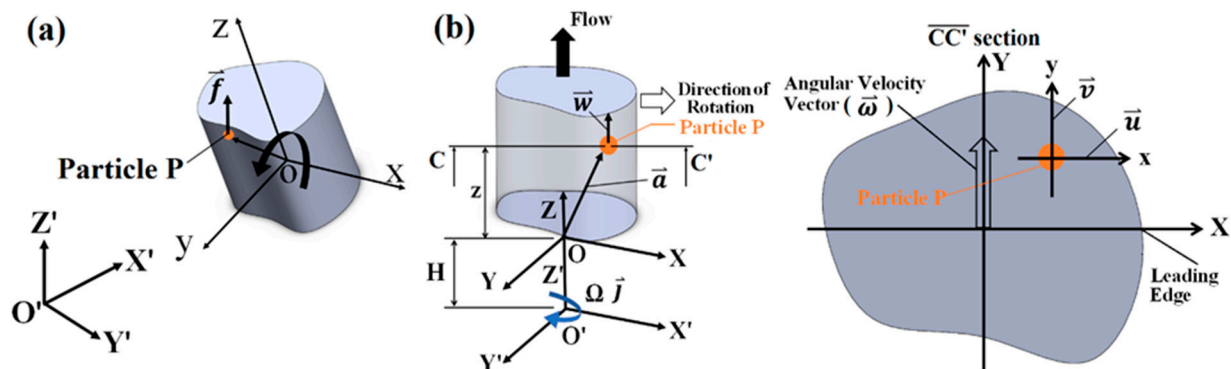


Figure 1. (a) a segmental flow passage of an arbitrary cross-section that rotates and translates with respect to an inertial reference frame $O'X'Y'Z'$. (b) fluid motion referring to a rotating Cartesian coordinate system, $OXYZ$, at a constant speed with an eccentricity H away from the origin $O'X'Y'Z'$ of an inertial frame of reference.

In Equation (1), $\partial \vec{a} / \partial t$ and $\partial^2 \vec{a} / \partial t^2$ are the velocity and acceleration of particle P with a mass m relative to the moving frame of reference $oxyz$. The direction of Coriolis acceleration (force), $2\vec{\omega} \times \partial \vec{a} / \partial t$ ($2m(\vec{\omega} \times \frac{\partial \vec{a}}{\partial t})$) perpendicular to $\partial \vec{a} / \partial t$ and $\vec{\omega}$ is in-phase (opposed) or opposed (in-phase) to the tangential velocity of rotation for a radially outward or inward flow. The centripetal acceleration (centrifugal force) specified as $\vec{\omega} \times (\vec{\omega} \times \vec{a})$ ($m(\vec{\omega} \times (\vec{\omega} \times \vec{a}))$) always acts radially inward (outward) regardless the flow direction in the duct. As specified by Figure 1b where the duct rotates around the y axis with an angular velocity, Ω , and has an origin $OXYZ$ located at a distance, H , from the inertial frame $O'X'Y'Z'$, the position (\vec{a}) and angular velocity ($\vec{\omega}$) vectors described by the moving coordinates $OXYZ$ are defined as Equations (2) and (3) with \vec{f}_0 in Equation (1) as Equation (4) where the coordinates of particles are specified as (x, y, z) with their unit vectors of \vec{i} , \vec{j} , and \vec{k} .

$$\vec{a} = x\vec{i} + y\vec{j} + z\vec{k} \quad (2)$$

$$\vec{\omega} = \Omega\vec{j} \quad (3)$$

$$\vec{f}_0 = -\Omega^2 H \vec{k} \quad (4)$$

By substituting Equations (2) to (4) into Equation (1) and referring the velocity components in x, y, z directions of the moving particle with velocity \vec{V} as u, v , and w , the acceleration of particles described by the moving coordinates (\vec{f}) yields:

$$\vec{f} = \left(\frac{\partial u}{\partial t} + 2\Omega w - \Omega^2 x \right) \vec{i} + \frac{\partial v}{\partial t} \vec{j} + \left(\frac{\partial w}{\partial t} - \Omega^2 (H + z) \right) \vec{k} \quad (5)$$

Considering the flow inside a rotating channel at a constant speed ($\frac{\partial \vec{\omega}}{\partial t} = 0$) as featured by Figure 1b, the Navier–Stokes treatment with the fluid motion referring to a rotating Cartesian coordinate system, $OXYZ$, at a constant speed, $\Omega\vec{j}$, with an eccentricity, $H\vec{k}$, away from the origin $O'X'Y'Z'$ of an inertial frame of reference, the momentum conservation equation described by the $OXYZ$ rotating frame yields [2]:

$$\frac{D\vec{V}}{Dt} = -\frac{1}{\rho} \nabla P + \nu \nabla^2 \vec{V} - 2\vec{\omega} \times \vec{V} - \vec{\omega} \times (\vec{\omega} \times [\vec{a} + H\vec{k}]) \quad (6)$$

The last term of centrifugal force in Equation (6) includes the translation acceleration between the inertial ($O'X'Y'Z'$) and rotating ($OXYZ$) reference frames due to eccentricity, H , as $\vec{\omega} \times (\vec{\omega} \times H\vec{k})$. In the early numerical studies of orthogonal-mode rotating flows without the buoyancy effect, a potential function, χ , which combines the pressure potential and hydrostatic centrifugal force field in terms of gradient χ , is often introduced to simplify Equation (6) to:

$$\frac{D\vec{V}}{Dt} = -\frac{1}{\rho}\nabla\chi + \nu\nabla^2\vec{V} - 2\vec{\omega} \times \vec{V} \quad (7)$$

With heat convection, the fluid density in a rotating channel is a spatial function linked with the temperature field in a form of state equation:

$$\rho = \rho_{ref}[1 - \beta(T - T_{ref})] \quad (8)$$

In Equation (8), ρ_{ref} and thermal expansion coefficient, β , are evaluated at a reference fluid temperature, T_{ref} , which is often selected as the fluid inlet temperature or the local fluid bulk temperature. As the centrifugal force in a coolant passage of a gas turbine rotor blade extensively exceeds earth gravity, the Boussinesq approximation is applied to the centrifugal force field to yield Equation (7) into Equation (9):

$$D\vec{V}/Dt = -1/\rho\nabla P^* + \nu\nabla^2\vec{V} - 2\vec{\omega} \times \vec{V} + [\vec{\omega} \times \vec{\omega} \times (\vec{a} + H\vec{k})]\beta(T - T_{ref}) \quad (9)$$

In Equation (9), the pressure field, P^* , involves the hydrostatic effect of centrifugal force term, $\rho_{ref}\chi$. The buoyancy force is motivated by a source term of $[\vec{\omega} \times \vec{\omega} \times (\vec{a} + H\vec{k})]\beta(T - T_{ref})$ in Equation (9) to affect the fluid motion. Substitution of the transformed dimensionless variables defined in nomenclature into Equation (9) generates the non-dimensional momentum equations in x, y, z directions of a rotating $OXYZ$ frame as Equations (10)–(12), respectively:

$$(\vec{V}^* \cdot \nabla)U = -\frac{\partial P'}{\partial X^*} - 2Ro\bar{\omega}W + Ro^2\beta(T - T_{ref})[\bar{\omega}^2 X^*] + \frac{\nabla^2 U}{Re^2} \quad (10)$$

$$(\vec{V}^* \cdot \nabla)V = -\frac{\partial P'}{\partial Y^*} + \frac{\nabla^2 V}{Re^2} \quad (11)$$

$$(\vec{V}^* \cdot \nabla)W = -\frac{\partial P'}{\partial Z^*} - 2Ro\bar{\omega}U + Ro^2\beta(T - T_{ref})[\bar{\omega}^2(\varepsilon + Z^*)] + \frac{\nabla^2 W}{Re^2} \quad (12)$$

The emerging dimensionless flow parameters in Equations (10)–(12) are evolved from the convective inertial, Coriolis, and rotating buoyancy forces as Reynolds (Re), rotation (Ro), and buoyancy (Bu) numbers, respectively. Referring to Figure 1b, with the length scale in the z (radial) direction far larger than that of the x (channel wise) direction, the rotating buoyancy number (Bu) is defined as $Ro^2\beta(T - T_{ref})\varepsilon$. When the channel length is sufficiently large, the eccentricity ratio, ε , is often defined from the mean radius of the rotating channel, R_m . The involvement of Bu (Ro) in the x -wise (z -wise) momentum balance equations of Equations (10) and (12) demonstrates the implicit buoyancy (Coriolis) force effect on the flow structure over the cross-plane (axial-plane), leading to the interdependent Bu and Ro impact on the heat-transfer and pressure-drop of a flow in a rotating channel.

The non-dimensional energy equation with the dimensionless fluid temperature as the primary variable takes the general form of:

$$\frac{D\eta}{Dt} = \frac{1}{RePr}\nabla^2\eta \quad (13)$$

When the local heat flux of a rotating duct is prescribed by the local convective heat transfer coefficient, h , the heat convection in a rotating channel is expressed using a local Nusselt number, Nu , taking the general functional structure of:

$$Nu = \Psi\{Re, Ro, Bu, Pr, \text{boundary conditions}\} \quad (14)$$

Equation (14) is hence adopted as a guide to formulate a numerical or experimental study of a coolant flow in a rotating channel. The boundary conditions in Equation (14) include the geometric features of a rotating channel and its HTE element. As the development of Coriolis vortices on the sectional plane of a rotating channel is confined by the constituent walls, the influence of rotation on its aerothermal performance varies with channel shape. For a non-circular rotating passage, the channel orientation relative to rotation vector affects the shape of its solid boundary that confines the Coriolis vortices, and hence is involved in the boundary conditions of Equation (14). With strong buoyancy interactions in a rotating passage, the spatial distribution of $\beta(T - T_{ref})$ or $\beta\Delta T$ is linked with the thermal boundary conditions imposed on the channel walls to affect the flow development and the cooling performance.

For emulating the realistic engine condition with Ro and Bu in the operation envelope of a gas turbine engine, these governing flow parameters derived from rotation are alternatively expressed by Equations (15) and (16):

$$Ro = \frac{Pd_h^2\Omega}{\mu RT_b} \frac{1}{Re} \quad (15)$$

$$Bu = \frac{(T_w - T_b)}{T_b} \varepsilon Ro^2 \quad (16)$$

The rotation number is proportional to fluid pressure, P , angular velocity of rotation, Ω , and the square of d_h ; however, it is inversely proportional to fluid bulk temperature, T_b , and Reynolds number, Re . Johnson et al. [3–5] fulfilled the NASA HOST program by increasing P to significantly extend Ro up to 0.4–0.5 by running the test rig at a speed of approximately 1000 rev/min. To control Ro at a realistic engine condition of approximately 0.5, Chang et al. [6] increased d_h to approximately three times that adopted by Johnson et al. [3–5] for further reducing the rotating speed to implement the infrared radiography method for measuring the full Nu map on a rotating surface. In Equation (16), while Ro is proportional to P as attempted by Johnson et al. [3–5], the most effective way to extend the Ro range is to increase d_h , as Ro is proportional to d_h^2 . Using a square two-pass channel with 45° ribs on the two opposite leading and trailing endwalls of the inlet and outlet passes as a standard channel geometry [6], the favorable agreements between the $\overline{Nu}/\overline{Nu}_0$ data generated by increasing P [5] and d_h [6] are reached as shown as Figure 2. The various attempts to raise Ro by either increasing P [5] or d_h [6] engendered similar heat transfer results, affirming the similarity law defined in Equation (14). A noteworthy feature in Figure 2a,d is the reversed Ro -driven heat transfer impediment to enhancement from the static-channel reference (\overline{Nu}_0) once Ro exceeds a critical value. Having extended the Ro range, an attendant Bu extension is acquired as Bu is proportional to Ro^2 in Equation (17). An implication of the favorable $\overline{Nu}/\overline{Nu}_0$ agreements between the heat transfer data generated at the various Re ranging from 5000–24,000 [5,6] in Figure 2 permits the normalized $\overline{Nu}/\overline{Nu}_0$ ratio to be a function of Ro and Bu for a set of thermal, flow, and geometric boundary conditions as illustrated in detail in [2,7].

Having identified the functional structure of Nu for a rotating coolant channel in Equation (14), the realistic engine conditions for an internal coolant channel in a gas turbine rotor blade can be specified in terms of Re , Ro , Bu , and geometrical/thermal boundary conditions. For the Brite-EuRam IV project funded by the European Community under the Industrial and Materials Technologies Programme (1998–2001), the target Ro for a commercial aerojet engine was approximately 0.2 (maximum). Including the military applications, Morris [1] consulted Rolls Royce and the Ministry of Defense (UK) for the typical ranges of coolant channel geometry, flow velocity, rotating speed, and wall/fluid temperature in real engine blade cooling channels to specify the real cooling conditions in terms of Re , Ro , and density ratio ($\Delta\rho/\rho = \beta\Delta T$) as 100,000 (maximum), 2.0 (maximum), and

1.1–1.7, respectively. The effective diameter and mid-span eccentricity of a coolant channel were in the respective ranges of 3–7 mm and 250–350 mm [1]. The ranges of the governing dimensionless flow parameters must be matched for emulating a realistic cooling condition in a gas turbine rotor blade.

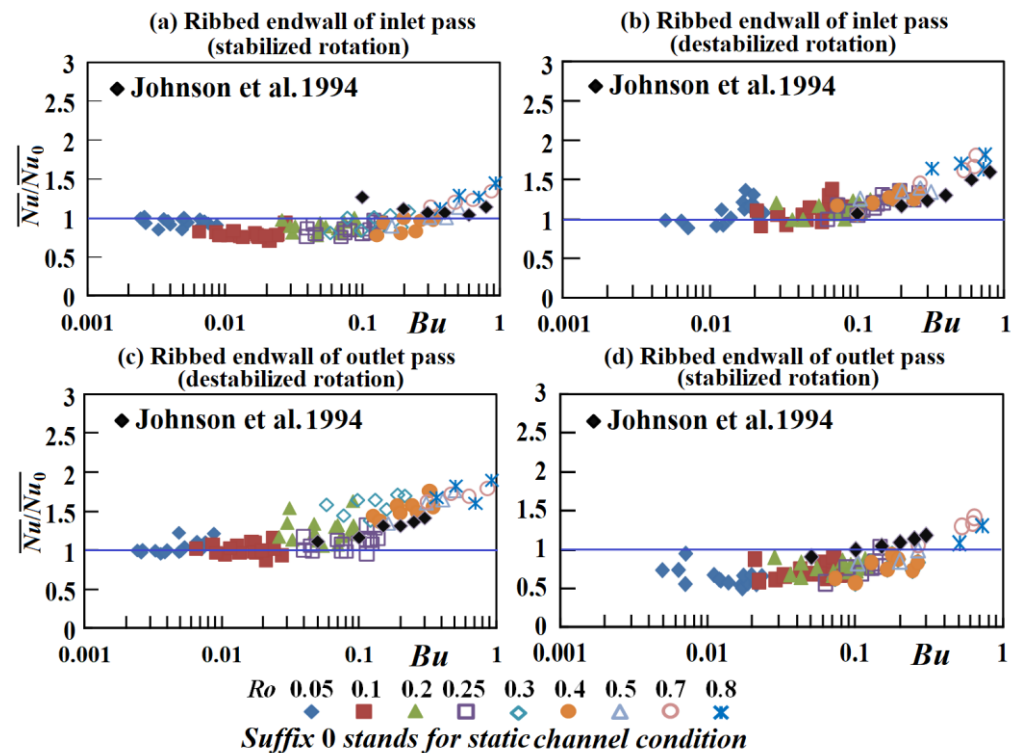


Figure 2. Comparisons of $\overline{Nu}/\overline{Nu}_0$ data generated by increasing P and d_h for the ribbed channels over the ribbed endwall of (a) inlet pass with stabilized rotation (b) outlet pass with destabilized rotation (c) inlet pass with stabilized rotation (d) outlet pass with stabilized rotation [5]. (Reprinted/adapted with permission from Ref. [6]. 2010, copyright Elsevier.)

3. Heat Transfer Enhancement of a Rotating Channel

As an effective measure to improve the power density and thermodynamic efficiency of a gas turbine engine, the increase in turbine entry temperature (TET) is constantly progressing to the current range of 1600–2200 K [8]. Based on the previous TET-increasing rate of 10 K/year, the long-term endeavor for advancing the internal cooling technology of a gas turbine blade plays a significant role in achieving an expected rate of 20 K per year in every mounting TET [9]. The HTE method for boosting the regional cooling effectiveness inside a gas turbine rotor blade generally accommodates blade geometry, its external heat flux profile, and the working thermal environment. The external flow structure along the flow pathway configured by the gas turbine blades results in a typical heat flux profile over the external surface of a gas turbine blade in Figure 3a. As reported in [10], the highest heat flux emerges at the stagnation point along its leading edge, at which point the hot gas flow is also agitated by the wake cutting disturbances from the upstream static turbine blade. Over the suction surface, the local heat flux decreases rapidly from the stagnation point due to the laminar boundary layer development. Further downstream, a laminar-to-turbulent boundary layer transition takes place on the suction surface to elevate the local heat flux. A turbulent boundary layer then proceeds up to the trailing edge of the turbine blade. Along the pressure surface of the turbine blade, a similar streamwise variation of heat flux is followed owing to the laminar-to-turbulent transition of the boundary layer. In the trailing-edge region of the pressure side, the additional flow complexities, including expansion waves, vortex shedding, and unsteady wakes, act with the turbulent boundary

layer to elevate the local heat flux as shown in Figure 3a. To ensure the aerodynamic efficiency of a turbine airfoil, its trailing edge is slim and structurally weak, which also limits the deployment of HTE elements in its internal coolant passage. In compliance with the typical heat flux profile of the external flow and the geometric characteristics of a gas turbine rotor blade, a typical internal cooling network is exemplified by a real gas turbine rotor blade as shown in Figure 3b.

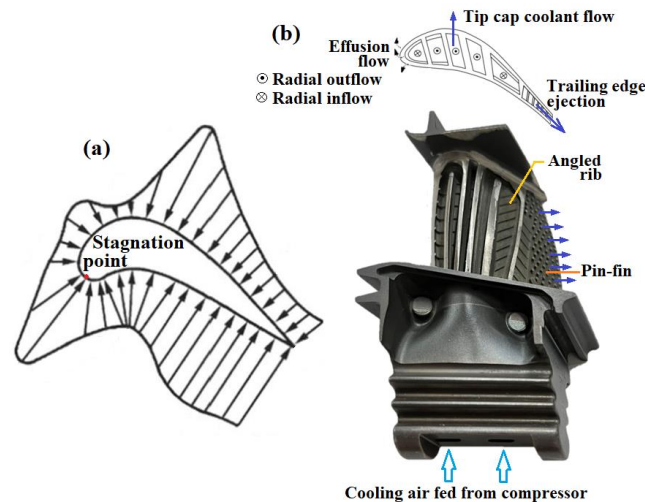


Figure 3. (a) typical heat flux profile over external surface (b) internal cooling network of a gas turbine rotor blade.

To cope with the high heat flux transferred from the surrounding gas around the stagnation point at the leading edge of a gas turbine rotor blade, the impinging jet with extremely high cooling effectiveness at the impingement spot is often deployed along the coolant channel in the leading edge of a gas turbine blade. Owing to the particular confinements of the spent flow, which is configured by the leading-edge coolant channel and the sealed channel hub or/and tip, the fluency of jet flow over the channel hub region is significantly undermined to deteriorate the local cooling effectiveness. Particularly, as the radially accumulative spent fluids after jet impingements are guided to flow in the hub-to-tip (radially outward) direction, the crossflow effect weakens the cooling effectiveness of the radially downstream jet by diffusing the jet momentum prior to impingement. The coolant ejects from the effusion holes to facilitate the film cooling by forming a clod layer of a gas-coolant mixture over the leading surface of the gas turbine blade. Furthermore, the fluency of spent flow in the leading-edge coolant channel is improved with the moderated crossflow effect, which act together to improve its internal cooling effectiveness.

As a set of illustrative examples for leading-edge cooling, Figure 4 depicts the Nusselt number maps of a trapezoidal channel cooled by an impinging jet row (a) without and with one, two, and three effusion rows in static conditions [11] and (b) with rotation for the non-effusion channel [12]. Over the hub region of the non-effusion channel in Figure 4a at zero Ro (static condition), the characteristic Nu_0 map with a high heat transfer zone around an impingement spot (stagnation point) of an impinging jet scheme is diminishing due to the significant jet flow confinement at the channel hub. At the channel tip, the considerable diffusion of the jet momentum by the strong crossflow obscures the Nu_0 peak at the impingement spot for the non-effusion channel. When the spent fluids are vented from the effusion holes to moderate the confinement and crossflow at the hub and tip regions, respectively, the cooling effectiveness of the impinging jet row is recovered. This is clearly visible in Figure 4a, where the high Nu_0 stripes are extended and intensified along with the advection of the spent flow in each effusion channel. Although the local cooling performance adjacent to the channel hub is noticeably improved from that without effusion compared with 4a, the unfavorable confinement effect remains persistent over the hub

region. When the centrifugal force is induced by rotation, the heat transfer recovery over the hub region of the non-effusion channel is systematically amplified as Ro increases from 0.05 to 0.3 in Figure 4b. The prevailing centrifugal force in the radially outward direction assists to improve the fluency of the spent fluid flow over the hub region.

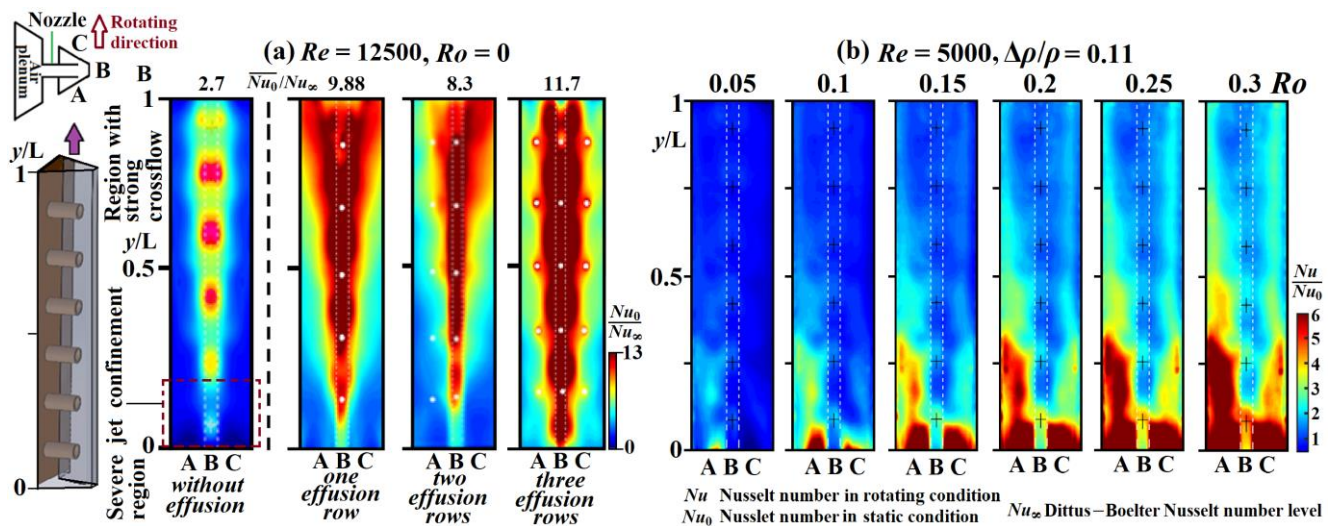


Figure 4. Nusselt number maps of a trapezoidal channel of an impinging jet row (a) without and with one, two, and three effusion rows in static conditions (b) with rotation for non-effusion channel. (Reprinted/adapted with permission from Ref. [12]. 2019, copyright Elsevier.)

Over the mid-chord region of a gas turbine blade, the space allowance for HTE elements in the coolant channels permits the ducted flow arrangement. As revealed by the early work that reported the evolution of gas turbine engines [13], the improvement of the internal cooling performance for the first static vane and rotor blade has led to a complex cooling flow geometry. Before the 1980s, the multi-hole cooling scheme with impingement and film cooling enabled the maximum turbine entry temperature (TET) to reach approximately 1100 °C [13]. The employment of serpentine ribbed flow and pin fin cooling schemes in the first stage turbine blade for a 1500 °C class industrial gas turbine AGT engine considerably raised its TET to be above 1350 °C [13]. As typified by Figure 3b, a serpentine passage with angled ribs is now commonly adopted for mid-chord cooling of a gas turbine rotor blade. While the consumption of coolant flow over the mid-chord region with the serpentine internal airway is significantly compared to those with a straight-through multi-hole internal cooling scheme, the different Coriolis force interactions with the radial outflows and inflows, as well as the flow complexities induced by the interconnected 180° sharp bends, add to the flow complications and urge for more fundamental research aimed at further improving its cooling performance. The most representative works in this regard include the experimental studies sponsored by NASA/the Lewis Research Center as part of the Host Section Technology (HOST) program [3–5]. Three four-pass serpentine rotating passages with smooth-wall, transverse, and 45° ribs were tested under realistic engine conditions. In order to alleviate the wall conduction effect on their heat transfer measurements, the isothermal heating condition was emulated. In the first outflow passage with normal and skewed ribs in static conditions, the Nu_0 levels on the ribbed endwall reached more than two and three times that of Nu_∞ . Between the skewed and normal trip rib floors, the Nu_0 values of the skewed trip duct were approximately 10 to 30% higher than those of the normal trip model due to the strong swirling flow caused by trips skewed at 45° to the bulk stream. For the three rotating four-pass channels with smooth-wall, normal, and skewed ribs, the qualitative heat transfer variations affected by rotation were similarly followed but the Nu levels were different. The rotating model with 45° ribs (smooth-wall) exhibited the highest (lowest) heat transfer rates on all duct walls.

Regarding the differential Bu effects among the three rotating models, their Nu data with 45° ribs implied a weakened buoyancy effect due to the better fluid mixing in trip channels so that the density perturbation ratio, $\Delta\rho/\rho$ or $\beta\Delta T$, is less a factor in heat transfer when the flow is well mixed in the channels with skewed trips [3–5].

In an attempt to develop the compound HTE method to further boost the cooling effectiveness of the mid-chord region of a gas turbine rotor blade, a two-pass furrowed channel with angled ribs on two opposite endwalls was recently proposed [14]. As illustrated by the conceptual flow structure in Figure 5a, the Coriolis forces are reversed in flow passes with radial outflow and inflow to alter the orientations of the counter-rotating Coriolis vortex in these flow passages. The periodic accelerated (decelerated) flow through the throat (bulge) section along each furrowed passage periodically alters the strength of Coriolis forces. Under a strong centrifugal force field with fluid density perturbations, the near-wall warmer fluids tend to be motivated toward the rotation center. The aforementioned synergetic buoyancy and Coriolis force effects on coolant motions results in skewed axial velocity profiles toward the trailing (TE) and leading (LE) endwalls in the rotating channels with radial outflow and inflow, respectively.

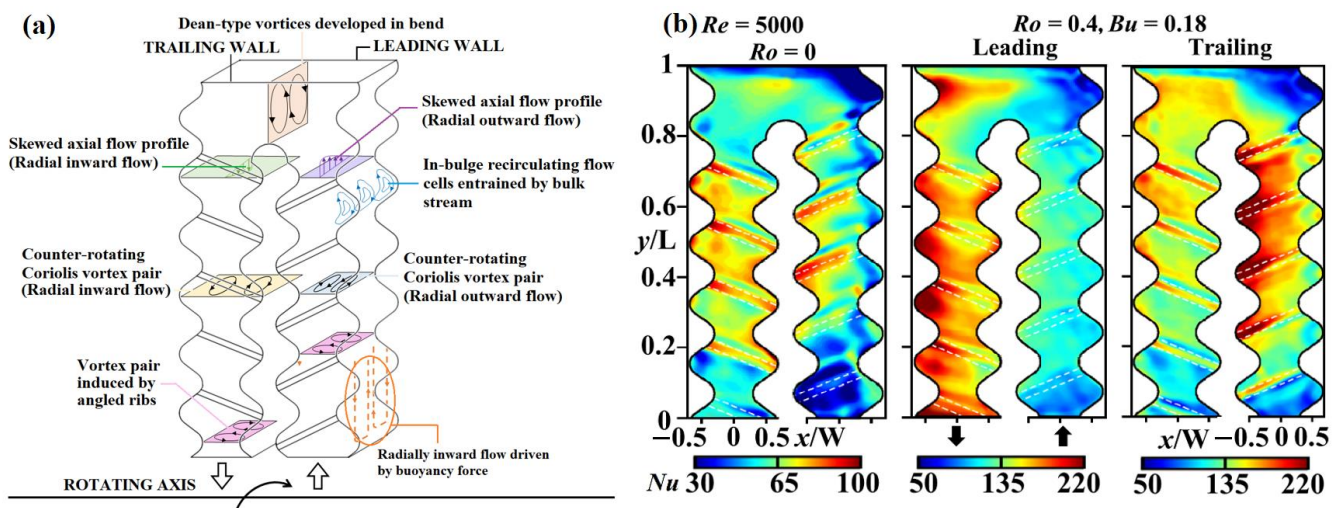


Figure 5. (a) conceptual flow structure (b) Nusselt number maps at $Ro = 0$ and 0.4 of two-pass furrowed channel with angled ribs. (Reprinted/adapted with permission from Ref. [14]. 2021, copyright Elsevier.)

As indicated in Figure 5a, the vortex pair induced by each pair of angle ribs is orthogonal to the Coriolis vortices. The protruded angle rib in each bulge along the two inner sidewalls disrupts the in-bulge recirculating flow cell to enrich the vorticity that boosts local heat transfer rates. The synergetic interactions among the flow structures induced by rotation, ribs, and the furrowed passage are further complicated in the sharp bend through which the Dean-type vortices are induced. The heat transfer responses to the flow structures without and with rotation are typified in Figure 5b. As well as a reconfirmation, the Nusselt numbers on the destabilized wall of the rotating LE (TE), namely the inflow second pass (outflow first pass) are raised above those on the stabilized endwall. Such endwall Nu differences between the destabilized and stabilized passes on the rotating LE or TE are dominated by the Coriolis force effect in promoting the turbulent activities over the unstable wall and the washing effect induced by the Coriolis secondary flows in Figure 5a.

The slim trailing edge of a gas turbine blade limits the selection of the HTE method with the increased external heat flux over the trailing-edge region in Figure 2b. The hot spots accordingly take place near the trailing edge of a gas turbine blade [15]. The merge of two flow streams along the pressure and suction surfaces of a gas turbine blade at its trailing edge, where the upstream wake-cutting effects also induce a periodic temperature field, often leads to localized thermal fatigue and turbine cracks. To maintain structure

integrity and material temperature at a sustainable level over the life span of a gas turbine blade, a pin fin array that bridges the two thin blade walls is customarily selected as the HTE element for trailing-edge cooling. In a pin fin channel, the periodical blockage of flow passage by the pin fins incurs the repetitive accelerating and decelerating flows to alter local pressure gradients and turbulent activities. Upon coolant impingement at the leading edge of a pin fin, the stagnation flow often accompanies the downstream vortices to merge with the vortical flows triggered at the separation point behind the pin. The streamwise advection of these vortices induces unstable shedding vortices to affect the endwall heat transfer properties. In particular, the localized flow instabilities at each pin endwall junction progresses with the re-developing boundary layers to generate horseshoe vortices which are lifted in the bulk stream to interact with the separated vortical flows behind each pin. Such vortical interaction often breaks down the coherent vortical structure into the small-scale vortices that enrich vorticity between two adjacent pin rows. A high heat transfer ring around each pin emerges on the channel endwall to reflect the localized HTE impact of the horseshoe vortices [16], whereas the endwall heat transfer promotions between two successive pin rows are associated with complex vortical interactions [17]. The flow impingement followed by the subsequent boundary layer re-development over a pin fin surface boosts the heat transfer rate on the pin fin surface which elevates the Nusselt number by approximately 35% of Nu_∞ on the pin surface [18].

The rich modes of vortical structures tripped among a pin fin array with extended cooling surfaces play a dominant role in its HTE effect. In view of lacking the cross-plane secondary flows, which prevail over the entire coolant duct with angled ribs, for a pin fin channel, the diamond-shaped pin row is mounted on a skewed rib land for further promoting the endwall HTE effectiveness [19]. The conceptual flow structure as well as the Nusselt number maps on LE and TE of the static and rotating channels with pin fins on skewed rib lands [19] are depicted in Figure 6a,b, respectively. In addition to the various vortical flows induced by pin fins, the rib-induced vortices act with the Coriolis vortices, which are orthogonally skewed with the vortices tripped by the angle ribs, considerably promote the core-to-wall fluid mixings. Such compound HTE treatment for trailing-edge cooling elevates the HTE effectiveness above those with pin fins or angled-ribs alone. The ratios of Nu_0/Nu_∞ in the rectangular channel with the diamond-shaped pin row between a pair of skewed ribs are raised to 6.1–5 with $5000 \leq Re \leq 15,000$, and the range is further extended from 1.5–3.8 for the channels with the pin fins and dimples [20], the parallel, crossed, and V-shaped angled ribs [21], the in-line diamond-shaped pin fins [22], and the staggered pin fin arrays with circular, cubic, and diamond shapes [23].

With rotation, the cross-plane Coriolis secondary flows interact with the various vortices tripped by ribs and pin fins as highlighted in Figure 5a to incur the Ro -dependent variations of the Nu distribution in Figure 6b. The typical Coriolis washing effect that motivates the warmer fluids from an unstable wall (TE) toward a stable wall (LE) in the rotating pin fin channel incurs the TE-to-LE Nu difference, which is enlarged with Ro . As a general Ro effect on heat transfer performance, the average Nu over an unstable wall (TE) consistently increases with Ro . On the LE (stable wall) of the rotating pin fin channel, the averaged Nu is initially reduced from the static-channel heat transfer references and recovered as Ro exceeds the critical value (Ro_{cr}), which is 0.1 for the pin fin channel. In Figure 6b on LE, the heat transfer recovery at $Ro \geq Ro_{cr}$ is initiated by raising Nu along the obtuse channel sidewall among the pin fin array. However, the locations of low Nu regions on the rotating leading endwall remain less affected by raising Ro . In [24] with $Ro < Ro_{cr}$, the Coriolis forces motivate the bulk flow toward (away) TE (LE) endwalls. The endwall HTE effect gaining from the near-wall vortices tripped at pin endwall junctions are promoted (weakened) on TE (LE) [19]. With $Ro \geq Ro_{cr}$, the returned Coriolis secondary flow from the TE (unstable endwall) gains sufficient momentum to revert the skewed bulk stream toward the LE (stable endwall) wall [25] to suppress the lifted near-wall flow on the rotating stable wall (LE), leading to heat transfer recovery. In the pin fin channel of Figure 6, the high Nu imprints are closely relevant to the vortices tripped at pin endwall

junctions. Thus, the Nu imprints on the LE generally follow the static-channel pattern. As $Ro \geq Ro_{cr}$, the values of ranges of high Nu rims around the pin fins on the LE extend with Ro , which has led to heat transfer recovery of the endwall average Nu . On TE in Figure 6b, the rib-wise and streamwise extensions of high Nu regions caused by raising Ro suggest the advanced Coriolis force-driven washing effect that pushes the near-wall vortices at pin endwall junctions toward the TE to incur its continuous Nu increase with Ro .

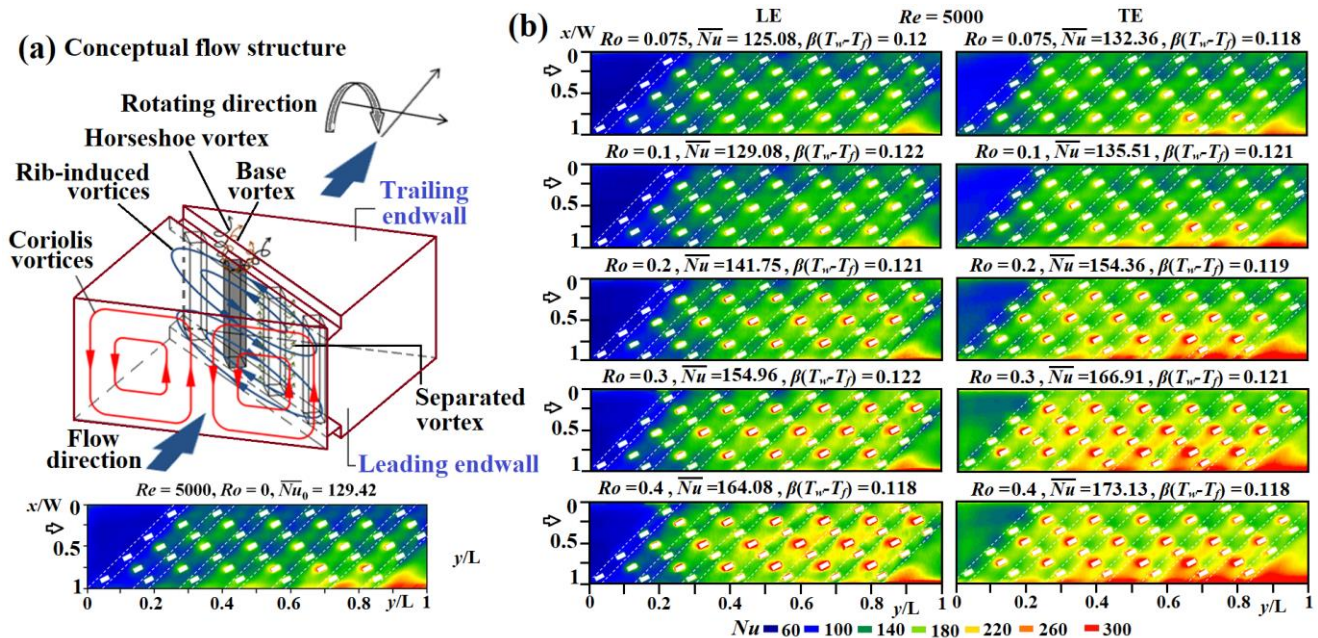


Figure 6. (a) conceptual flow structure and (b) Nusselt number maps on LE and TE of static and rotating channels with pin fins on skewed rib lands. (Reprinted/adapted with permission from Ref. [19]. 2014, copyright Elsevier.)

While the general Ro (Coriolis force) effects on the heat transfer performances of rotating channels follow the aforementioned data trends, the quantitative differences exist among different rotating channels with various geometrical and HTE configurations. Along with the advancements of manufacturing technologies, the more complicated HTE devices, evolving from the conventional internal cooling network featured in Figure 2b, are attempted with their aerothermal performances assessed in realistic engine conditions. The following literature review summarizes the main findings of recent studies for leading-edge, mid-chord, and trailing-edge cooling of a gas turbine rotor blade.

4. Leading-Edge Cooling

4.1. Rotating Channels with Impinging Jets

With diminished boundary layers at the stagnation (impingement) point on a target plate of a jet flow, the localized high heat transfer rate of an impinging jet is utilized to counteract the peak external heat flux along the leading edge of a gas turbine rotor blade as featured in Figure 2a. Hsieh et al. [26] examined the effect of impinging jet location on the heat transfer performance of the rotating ribbed channels. Rotation suppressed the heat transfer performance from those without rotation. While there was 20–30% heat transfer enhancement by the transverse ribs, the HTE impact induced by the square rib was higher than that with a semi-circular rib. Adreini et al. [27] adopted the steady-state liquid crystal method to measure the Nu map on the internal concave surface of a rotating channel with impinging jets to reveal the effects of different mass flow extraction from the pressure and suction side at two crossflow configurations corresponding to 70% (blade hub section) and 10% (blade tip section) of the total cooling flow. The effects of the extraction hole area and position on heat transfer performance, both in terms of averaged Nu levels and local Nu

distribution, were secondary with respect to the jet Reynolds number and crossflow ratio. This research group also investigated the cold-bridge-type leading-edge rotating channel with impinging jets emitted from a cavity and spent air extracted through five rows of effusion holes [28]. The heat transfer characteristics were dominated by the jet Reynolds number, whereas the jet ejection and extraction conditions affected the distribution patterns of Nu maps. Rotation tended to undermine the cooling performance, and such an effect was an augmented increase as crossflow diminished. Furlani et al. [29] conducted the flow measurements of an advanced leading-edge cooling channel with multiple impinging jets and coolant extraction by means of 2D and Stereo PIV in static and rotating conditions at an Ro of 0.05. The Ro (Coriolis force) effect on the jet structure was not significant but caused a strong crossflow deflection toward the trailing wall (pressure side) that enhanced in magnitude from hub-to-tip sections. Near the channel tip, the unbalanced flow field toward the suction side of the feeding channel was strong enough to sustain a recirculating region downstream of the central jet hole. Elston and Wright [30] studied the effect of rotation on the cooling performance of an impinging jet row in a smooth square channel, with the jets impinging on a semi-circular concave surface and the spent flow expelled through effusion holes. With pure jet impingement, the deflected impinging jet co-acts with the secondary flows induced by rotation to augment fluid mixings in the impingement cavity that promote its cooling performance. With a strong crossflow, the Nusselt numbers in static and rotating channels were similar. Singh and Ekkad [31] studied the effects of Coriolis force and centrifugal buoyancy on heat transfer of a rotating dimpled channel with impinging jets using transient liquid crystal thermography. The rotational effect was beneficial for enhancing heat transfer on leading and trailing walls for the smooth-walled channel but exerted negative effects on heat transfer enhancement over the dimpled target surface. The higher Nusselt numbers emerged on the leading wall in the impingement dominant regime, but this effect was diminished with the increased strength of the crossflow. Chang and Yu [12] used infrared thermography to detect the endwall Nu maps and Fanning friction factors of the rotating trapezoidal channel with an impinging jet row at a channel orientation of 45° from the rotating axis. Acting by the Coriolis forces on the radially outward crossflow and the impinging jets, the airflow rates issued from the jets adjacent to the channel hub (tip) were increased (decreased) compared with those in the static impinging channel. The deteriorated heat transfer performance over the cavity-like channel hub region was considerably improved by the rotational force. The rotating buoyancy effect impaired cooling performance, but its effect was weakened as Ro increased. Wang et al. [32] measured the local Nusselt numbers in a rotating rectangular channel with impingement jet and effusion holes at a jet rotation number (buoyancy number) which varied from 0–0.24 (0–0.57) for three channel orientation angles of 90° , 135° , and 180° . At a channel orientation angle of 135° , the Coriolis force deflected the jet and undermined the regional cooling performance. The distribution patterns of Nu were not obviously modified by Bu but were sensitive to the channel orientation angle owing to the altered Coriolis flow structures and the different bending direction for the impingement jet. Deng et al. [33] studied the rotational effects on the cooling performance of a rotating channel with impinging jets and air extraction with the aid of flow simulation results. The cooling effect on the suction side was superior to its pressure-side counterpart. The non-uniform jet flow variation deteriorated the cooling performance from channel tip-to-hub sections. Rotation boosts the non-uniformity of mass flux, resulting in a local heat transfer increase by 140% over the hub region on the pressure surface. This research group then focused on the effect of channel orientation on the jet flows and their heat transfer performances [34]. With the channel orientation angle between 90° and 135° , the Coriolis force induced a large vortex in the feeding channel to alter the mass flux distribution of the jet flow. Cooling performances in the middle and both channel ends were, respectively, undermined and promoted. When the channel orientation yielded to 135° – 180° , the stagnation heat transfer zone decreased with Ro . The jet diversion induced

by rotation became the primary factor for heat transfer impediments, yet the jets were also driven away from the impinging wall at high Ro .

4.2. Rotating Channels with Swirl Chamber

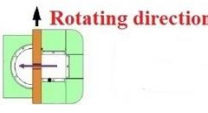
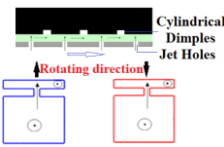
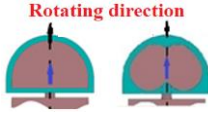

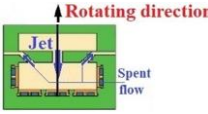
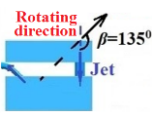
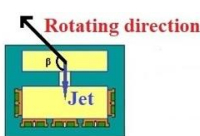
Gleze et al. [35] pioneered the effect of rotation on heat transfer in a screw-shaped swirl chamber for leading-edge cooling in a gas turbine rotor blade. The Coriolis force promoted (undermined) cooling effectiveness when its direction coincided (opposed) with the tangential velocity of the swirling flow. The centrifugal buoyancy effect was negligible for the overall cooling effect but led to redistribution of the Nusselt number. Rao et al. [36] reported a comparative study for the heat transfer and pressure loss characteristics in the rotating swirl tubes with one (S1) and five (S5) tangential inlet jets under equal overall mass flow rates and inlet jet Reynolds numbers, respectively. With similar overall mass flow rates, the heat transfer and pressure loss coefficients for the S1 swirl tube were significantly higher than the swirl tube S5. However, the swirl tube S5 exhibited a more uniform heat transfer distribution along the swirl tube. With similar jet Reynolds numbers, the tube average Nu of swirl tube S5 exceeded its S1 counterpart. The crossflow effect was not detrimental to the heat transfer performances in the S5 swirl tube. Wang et al. [37] carried out a numerical study to explore the effects of jet hole shape and channel geometry on leading-edge impinging cooling channels in static and rotating conditions. The impinging jet issued from the racetrack-shaped hole effectively persisted under an intensive crossflow to promote cooling performances. Their double-swirling chamber channel lessened the adverse Coriolis force effect with considerable HTE impacts and uniform temperature distributions. As Ro increased, the Nusselt numbers on the LE and TE decreased with Ro , in particular with high Re . Tansakul [38] numerically studied the buoyancy effect on the cooling performance of a rotating double-swirling chamber in engine realistic conditions using SST $k-\omega$ turbulence models. With the twin swirls induced by the spent fluid flows of the central impinging jet, the Nu peak constantly developed at the stagnation point along the periphery of the rotating target wall. The buoyancy effect yielded the peripheral Nu profile to be asymmetric at the impingement point and undermined the channel average Nu and thermal performance factor by 40.43% and 39.80%, respectively. The impaired cooling performance by the buoyancy effect in rotating conditions suggested the significance of buoyancy force for designing the particular double-swirling chamber in the leading edge of a gas turbine rotor blade. The reported Nu/Nu_0 ratios, f/f_0 ratios, and the corresponding tested Re , Ro , and Bu ranges of the rotating channels applicable to the leading-edge cooling of a gas turbine rotor blade are summarized in Table 1.

In [12,26–35], the works focused on leading-edge cooling of a gas turbine rotor blade, the reported results involving the parametric analysis with the depictions of Ro -driven Nu/Nu_0 variations are compared in Figure 7. The test conditions in terms of Re , Ro , Bu , and the accompanying heat transfer and/or pressure drop results are summarized in Table 1. The flow through an internal coolant channel embedded in the leading edge of a gas turbine is mostly radially outward. As a result, the direction of Coriolis force in a rotating channel with impinging jets or swirls in Figure 7a is counteracting with the direction of rotation. In Figure 7a, the channel orientation is normal for the rotation vector. The conceptual vortical interactions between the Coriolis vortices and the flow cells induced by the spent flow after impingement or the swirl in Figure 7a remains applicable at different channel orientations. However, the symmetric vortex pair generated by the Coriolis forces in Figure 7a yields to an asymmetric pair owing to the asymmetric profile of a channel wall relative to the Coriolis forces when its orientation is tilted from the scenario depicted in Figure 7a.

In Figure 7a with jet cooling schemes, the impinging jet emitted from an extended nozzle tube [12] or the orifices through the interior channel wall [28–31] induce the vortex pair on the cross-section of a rotating channel. While the structure of the jet induced vortex pair is similar, the diffusion of jet momentum by the radial outward crossflow along the channel with the jet formatted through the orifice in the interior channel wall is expected to be more severe than when the jet is emitted from an extended nozzle tube.

For a swirl chamber cooling scheme, the single-cellar or twin-cellar vortices are induced by the tangential or middle entry flow which swirls in a radially outward direction along the coolant channel. With a radial outward flow, the Coriolis secondary flows follow a similar pattern for the rotating channel with a particular shape. With an impinging jet cooling scheme, the Coriolis vortices are orthogonal to the jet-induced vortices, while the orthogonal, or co-acting, or counteracting vortical flows between the Coriolis vortices and swirling flow cells interact depending on the entry flow arrangement for a rotating swirl chamber. As a result, a variety of regional vortical destruction or promotion between the Coriolis vortices and the flow cells induced by jets or swirls generate different trends of Nu/Nu_0 variations against Ro in Figure 7b.

Table 1. Tested conditions, heat transfer, and pressure drop results of rotating coolant channels adopted for leading-edge cooling of a gas turbine rotor blade.

Cooling Geometry	Re	Ro	$\Delta p/\rho (\beta \Delta T)$	Bu	Nu/Nu_0	Nu_0/Nu_∞	f/f_0	f_0/f_∞	Ref.
	10,000–40,000	0–1.4	-	-	0.7–1.3	-	-	-	[30]
	2500 (jet)	0–0.00274 (jet)	-	-	0.51–1.37	-	-	-	[31]
	7854–19,635	0–1.9557	-	-	0.18–0.98	0.9–1.42	-	-	[37]
	5000–17,500	0–0.3	0.057–0.151	0–0.088	0.5–4.6	-	0.9–1.1	16–23	[12]
	5000–10,000	0–0.24	-	0–0.57	0.76–1.24	1.1–4.2	-	-	[32]
	5000	0–0.24	-	0–0.57	0.3–2.75	0.55–4.3	-	-	[33]
	5000–15,000	0–0.24	-	0–0.2	0.25–2.25	-	-	-	[34]

Suffixes $_0$ and $_\infty$, respectively, refer to the zero-speed (static) condition and the results evaluated from D-B and Blasius correlations.

For the impinging jets emitted through the orifices in the divider wall [30,32–34], the stronger crossflow effect undermines the HTE effectiveness of the impinging jet. The higher Nu/Nu_0 ratios for the trapezoidal rotating channel with the impinging jets emitted from the extended nozzle tubes in Figure 7b are noted. In [12], the almost-stagnant spent flow confined by the sealed hub section resulted in a low Nu_0 zone as indicated in Figure 4a. With rotation, the centrifugal forces in a radially outward direction improve the fluency of the stagnant-like flow structure entrapped in the hub region of the rotating trapezoidal

channel to significantly recover the regional cooling performance, leading to the systematic elevation of the regional Nu/Nu_0 ratios as Ro^2 increases in Figure 4b. The high area average Nu/Nu_0 ratios in Figure 7b for the rotating trapezoidal impinging jet channel is attributed to the high Nu/Nu_0 ratios adjacent to its sealed channel hub as demonstrated in Figure 4b, whereas the local Nu/Nu_0 ratios near the opened tip end of the non-effusion channel fall in the range of 1–1.5. For the swirl chamber with the particular channel shape shown in [37], its Nu/Nu_0 ratios are in the range of 0.3–1 in Figure 7b, which are slightly less than the data generated in the rotating impingement channel [30].

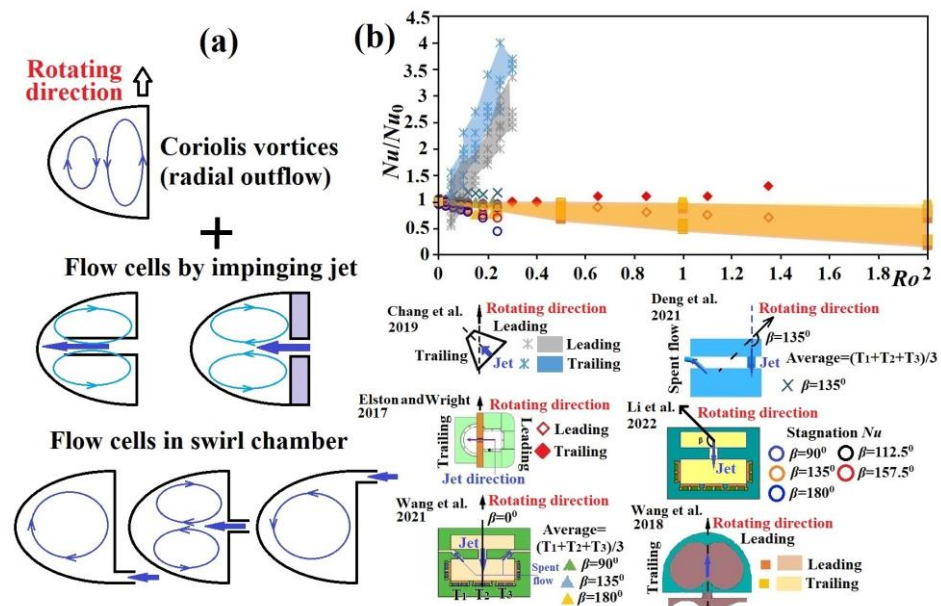


Figure 7. (a) conceptual flow structures on the cross-section of a leading-edge rotating coolant channel (b) variations of Nu/Nu_0 against Ro for the rotating channels typical in the leading edge of a gas turbine rotor blade using impinging jets and swirl chambers [12,30,32–34,37].

5. Mid-Chord Region Cooling

In the mid-chord region of a gas turbine rotor blade, the orientation and shape of an internal coolant channel are varied in the chord-wise direction to fit the interior geometry of the airfoil. Rectangular channels with different channel width-to-height ratios (aspect ratios, AR), parallelogram channels, and trapezoidal channels are widely deployed in the cooling network over the mid-chord region. As the periphery of a rotating channel confines the sectional vortical flows induced by the Coriolis forces, the aerothermal performance of a non-circular rotating channel is affected by its shape and orientation. The effects of channel shape, orientation, and HTE elements on the aerothermal performance of a single- or multi-pass rotating channel are extensively studied. In particular, the serpentine coolant passage is in common use for saving the coolant consumption over the mid-chord region. Apart from the saving initiative of coolant consumption, a multi-pass channel was attempted for taking the HTE advantages attributed to Coriolis forces by configuring its coolant walls in contact with the hot gas as the unstable sides of the flow passages with radial outflow and inflow [39]. It is noted that this cooling concept is mostly applicable for mid-chord region cooling. The data generated by our research group [39] is reprocessed from Nu/Re^n to Nu/Nu_0 for highlighting the effects of rotation on the two unstable sides of the flow passages. In Figure 8a, the two-pass channel is separated by the central divider to construct the entry (exit) pass with radial outflow (inflow). The unstable channel walls toward which the core cold coolant is directed by Coriolis forces in these two rotating passes are adjacent to the hot gas to take advantage of the HTE benefits from the Coriolis forces. In Figure 8b, all the heat transfer levels on the channel hot walls at the channel

orientation angles of 0° and 45° keep increasing with Ro from $Ro = 0$ to $Ro = 1$ along the rotating two-pass trapezoidal ribbed channel.

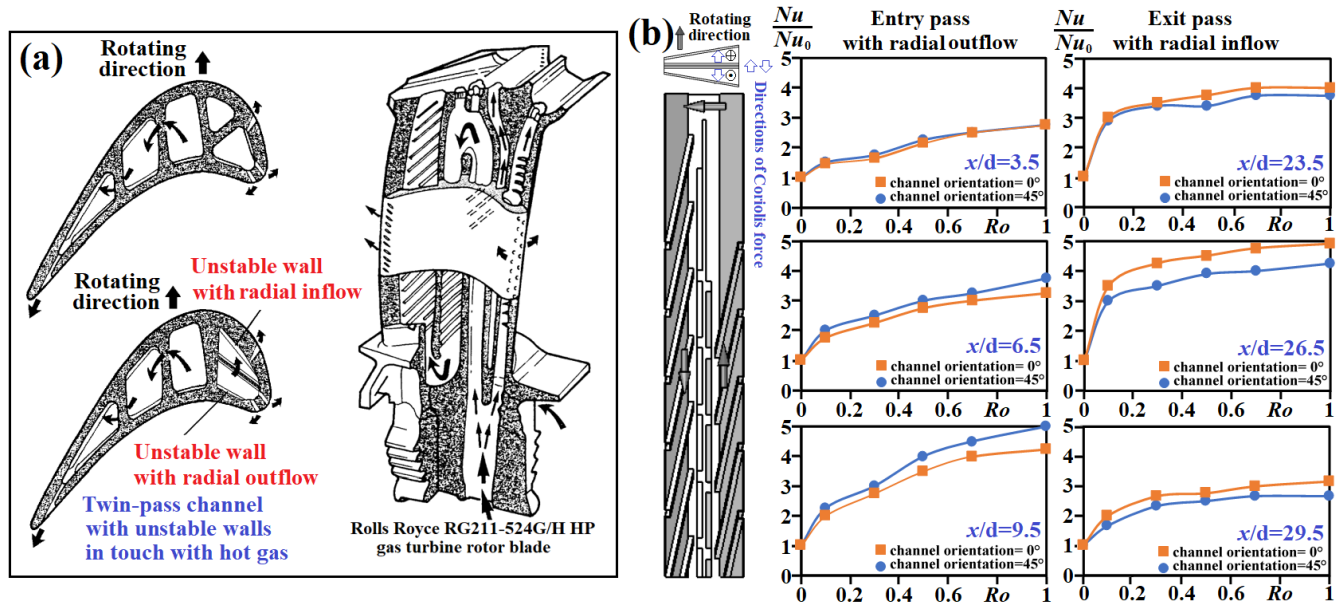


Figure 8. (a) Internal cooling concept for utilizing a positive HTE Coriolis force effect by installing a twin-pass trapezoidal channel in a gas turbine rotor blade (b) variations of normalized Nusselt number against Ro at different axial locations demonstrating the improved cooling effectiveness with Ro .

Recently, Guo et al. [40] suggested positive utilization of the Coriolis force effect to boost the cooling effectiveness on the heated channel wall as the Coriolis-utilization rotating condition to investigate the flow structures and heat transfer characteristics of a rotating smooth two-pass U-channel in stationary, conventional rotating, and Coriolis-utilization rotating conditions. In Coriolis-utilization rotating conditions, the heat transfer elevations from Nu_0 references were found on both leading and trailing walls, and the pressure drop penalties were also reduced compared with those in conventional rotating conditions. The multi-pass channel featuring the Coriolis-utilization rotating condition was recommended as a promising internal cooling scheme for future works. In the next section, the literature exploring the cooling performances of the rotating channels with rectangular, non-rectangular, and the realistic multi-pass arrangement of variant sectional shapes are summarized.

5.1. Rotating Rectangular Channel

Chang and Morris [2] attempted to uncouple the Coriolis and centripetal buoyancy force effects on local Nu along the centerline of the rotating, ribbed, leading, and trailing wall of a rotating square duct. For this rotating ribbed duct, the isolation of forced heat convection from Coriolis and buoyancy effects using the Re scaling idea with the Re exponent determined from the non-rotating Nusselt number correlation was permissible. The uncoupled Coriolis force effects caused the heat transfer impediment over the leading wall, and it promoted heat transfer rates on its opposite trailing wall. As an early work for mid-chord cooling of a gas turbine rotor blade using multi-pass channels, Han et al. [41] carried out a numerical study to investigate the rotational effects on the flow and heat transfer in the two-pass channels with aspect ratios (channel width-to-height ratio, AR) of one, two, and four. For all the rotating channels with different ARs, a pair of counter-rotating vortices perpendicular to the bend-induced vortices was generated by the Coriolis force that led to the growth of the vortex near the leading surface of the bend. Such leading surface vortex was vertically expanded as the AR was reduced from 1 to 1/4. The effects of rotation on heat transfer were more pronounced for the channels with low

ARs. Liou et al. [42] measured the centerline of Nu on the leading and trailing endwalls roughened by the 45° staggered ribs of three rectangular channels with $AR = 1, 2$, and 4 at Reynolds (Re), rotation (Ro), and buoyancy (Bu) numbers in the respective ranges of 5000 – $30,000$, 0 – 2 , and 0.005 – 8.879 . Without rotation, the centerline Nu increased with the AR due to the increased rib-height to channel-height ratio. When Ro increased to two, the past experiences [43–45] that investigated the AR effects on the heat transfer performances of rotating ribbed channels were not applicable in the high Ro range ($Ro > 1$). The increase in Bu elevated the Nusselt number ratios, Nu/Nu_0 , in the rotating square ($AR = 1$) channel but impaired the heat transfer rates in the channels with $AR = 2$ and 4 . The critical Ro above which the Nu/Nu_0 ratio turned to be increased with Ro on the stabilized leading ribbed wall emerged at 0.1 for the channels $AR = 1, 2$, and at 0.3 in the channel of $AR = 4$. While all Nu/Nu_0 ratios on the destabilized trailing ribbed wall increased with Ro , the Ro -driven heat transfer increases toward the increase in AR were less systematic.

Chang et al. [46] firstly adopted the infrared thermography method to measure the full-field Nu maps of a rotating channel. The leading and trailing walls were configured as skewed sinusoidal waves. The endwall Nu distributions of the rotating rectangular channel were measured at $Ro = 0$ – 0.22 , and $Bu = 0.003$ – 0.11 . The Nu/Nu_∞ ratios on the rotational leading and trailing walls reached 3.4 – 4.3 and 4.2 – 6.4 , respectively, to grant the potential applicability of the wavy channel as an HTE element for the cooling of a gas turbine rotor blade. Using the conventional thermocouple method, Chang et al. [6] also measured the endwall Nu maps of a rotating two-pass square channel with leading and trailing endwalls roughened by 45° staggered ribs at the Re , Ro , and Bu in the respective ranges of 4000 – $16,000$, 0 – 0.8 , and 0.0015 – 0.93 ($0.05 \leq \Delta\rho/\rho \leq 0.1$). On the rotating destabilized endwalls, namely the trailing and leading walls of the inlet and outlet passes, the endwall average Nu increased with Ro , while their stabilized counterparts were initially reduced and followed by a subsequent increase. The critical Ro above which the heat transfer impediment from Nu_0 turned to be increased with Ro was 0.1 for the rotating flow configuration. At $Ro > 0.5$, the ratios of average Nu/Nu_0 on the rotating stabilized walls reached above unity. In the straight ribbed inlet and exit passes, the patterns of endwall Nu distributions were manifested by Ro . However, the Nu distributions on the bend endwalls became Ro and Re dependent. The interdependent Re and Ro effect on the cooling performance of the rotating bend was relevant to the Re -associated Dean-type vortices that interacted with the rotation-induced flow complexities. While the patterns of endwall Nu distributions were governed by Ro and Re for the rotating bend, the enhancing or impairing Bu effect on local Nu was observed over the leading and trailing walls of the rotating tow-pass ribbed channel.

Mayo et al. [47] measured the flow and endwall Nu map of a rotating square duct with 90° ribs in realistic engine conditions. The turbulence profiles and secondary flows modified by rotation affected the distribution pattern of Nu and its average value. On the trailing ribbed floor, the turbulence promotion co-acted with the Coriolis vortices to flatten the Nu profile and raised the averaged Nu as Ro increased. On the leading ribbed wall, the Coriolis secondary flows counteracted the turbulence reduction to exhibit a limited decrease in its overall Nusselt number. Xu et al. [48] focused on examining the rib-pitch effect on Nu and f in a rotating two-pass square ribbed channel. The transverse rib pitch-to-height ratios in the entry pass with radial outflow varied from 3.8 to 14.4 but remained at 10 in the exit pass for the radial inflow. The more pronounced rib-pitch effect was found in the entry pass, in comparison with that in the exit pass. The flow intricacies induced by rotation moderated the rib-spacing effect. The rib pitch-to-height ratio of 10 generated the best HTE performance among the comparative groups, except on the trailing wall of the entry pass.

Wang and Corral [49] explored the effect of uneven wall heating conditions on flow and heat transfer performance in a rotating channel with one channel endwall roughened by 45° ribs. At a high Bu , the buoyancy effect was considerable. The trailing endwall Nu at the four-wall heated condition was significantly higher than those with only the ribbed wall

heated. However, the heat transfer sensitivity to the heating conditions was inconspicuous over the leading ribbed wall. Deng et al. [50] measured the pressure drop and heat transfer coefficients of a rotating two-pass channel with 45° ribs at a Ro that reached 1.02. The HTE effect of the 45° ribs on leading and trailing walls promoted 40–80% (15–65%) Nu elevations on ribbed endwalls (smooth sidewalls). Compared with the smooth channel, the f factors were raised by approximately 150–210%, and the penalty decreased with Re . Yet, the rotation-to-stationary f ratios decreased with Ro in rotating conditions of $Ro < 0.55$, above which the Ro -driven f increase was triggered. The ribbed-to-smooth TPF ratio was significantly elevated by rotation when Ro exceeded 0.25. Singh et al. [51] suggested that the combined effects of Coriolis force and buoyancy in a rotating passage often led to non-uniform cooling effectiveness in a conventional multi-pass rotating channel, and this research group attempted to utilize the Coriolis force favorably by turning the conventional two-pass channel 90° . The Nu maps were reported at $Re = 20,000$ and $Ro = 0$ and 0.1 . The combined experimental and numerical findings supported the proposed design concept with an 11% higher HTE ratio at 8% lesser pumping power compared with the conventional two-pass ribbed channel. Wang et al. [52] numerically studied the effects of discrete skew-rib configurations on the heat transfer and fluid flow characteristics in a rotating rectangular channel ($AR = 2:1$) at five channel orientations. The small streamwise rib gap promoted the HTE effectiveness on the leading wall, but the HTE impact was decreased by enlarging the streamwise rib gap. A widthwise rib gap was favorable for reducing f with limited HTE improvements. Yan et al. [53] numerically studied the effusion effects on the internal cooling performance of a rotating ribbed two-pass channel. The results highlighted the considerable impact of effusion location on the pattern of Nu distribution over a rotating surface, whereas the mass flux through the effusion hole was varied distinctively by rotation. The heat transfer impact of rotation was mainly caused by the Ro effect on the flow reattachment and the secondary vortex structures.

In addition to rib turbulators for HTE augmentation in a rotating channel, the impinging jets and dimples were simultaneously attempted. Li et al. [54] compared the cooling performances of the single impinging jet row in a straight duct and the forced convection in the serpentine ribbed channel in rotating conditions. In the rotating conditions tested [54], the Coriolis force effects promoted serpentine cooling but weakened jet impingement cooling. Kim et al. [55] reported the detailed endwall Nu distributions of the rotating smooth and dimpled rectangular channels at two channel orientations of 90° and 120° using the transient liquid crystal technique. Results show that the heat transfer coefficient on the trailing surface was higher than that on the leading surface. At the 120° channel orientation angle, a higher heat transfer coefficient was observed near the outer surface. In the dimpled channel, the effect of the Coriolis force-induced secondary flow on the heat transfer performance was not as significant as that in the smooth channel. The heat transfer levels near the outer sidewall of the smooth channel with 120° channel orientation were raised compared with those near the inner sidewall due to the flow reattachments of the Coriolis vortices over the outer-trailing and outer-leading walls. With dimples at the channel orientation of 90° , the Coriolis force effect on the cooling performance was weakened compared with those with smooth walls. The flow interactions between the shifted core flow driven by Coriolis forces and the flow complexities tripped by dimples further promoted the HTE effectiveness on the trailing wall of the rotating channel. Lamont et al. [56] adopted the transient liquid crystal thermography to measure the Nu maps of rotating serpentine channels with single impinging row jets. The typical Coriolis force effect promoted (suppressed) Nu on the destabilized trailing wall (stabilized leading wall). Acting by the Coriolis force effect on the developing length of the potential jet core, the impinging jet heat transfer characteristic was modified. The unfavorable crossflow effect was enhanced at a smaller channel-height to jet-diameter ratio. Instead of using the concave dimple cavity as an HTE element, Chang et al. [57] explored the influence of rotation on the cooling performance of a rectangular channel enhanced by the hemispherical protrusions at high rotation numbers. Due to the separated vortices tripped at the apex of each hemispherical protrusion, the

endwall average Nu_0 reached 3.8–3.2 times Nu_∞ at Re between 5000 and 12,500. The Nu level on the destabilized (trailing) wall consistently exceeded that of its stabilized (leading) wall, whereas the leading Nu/Nu_0 ratio was reduced from 1 to 0.7 as Ro increased from 0 to 0.1, but recovered to be greater than unity as Ro reached 0.3. The isolated Bu effect for this rotating channel with the hemispherical protrusions, which was systematically weakened with Ro , promoted the cooling performances on the leading and trailing walls. Xu et al. [58] measured the heat transfer rates on the leading and trailing walls of a rotating rectangular ($AR = 4$) channel with dimples and sidewall bleeds at Ro (Bu) in the range of 0–1.24 (0–3.86). Without rotation, the channel averaged Nu_0 was elevated by 85.4–59.1% in the Re range of 5500–25,000 with diminished Bu effect. The rotational effect was weakened by dimples, yet Bu exhibited the positive heat transfer impact.

Instead of adopting the surface enhancement method to promote the HTE effectiveness of a rotating channel, Chang et al. [59] was inspired by the sharp zig-zag channel [60] to propose the S-shaped channel as an HTE alternative. When coolant travelled along an S-shaped channel, the direction of the centrifugal forces induced by the turning motion of the bulk stream reversed periodically to induce the multi-cellular flow structures on the channel cross-section. Without surface enhancements, the combined effects of Re , Ro , Bu , and the promoted fluid mixings by the secondary vortices induced along the S-shaped flow pathway raised the area average Nu on the leading (trailing) endwall to 3.17–6.83 (3.22–6.92) times Nu_∞ , leading its TPF values to be 1.25–2.04. This research group also combined skewed ribs and the wavy-shaped flow passage to further boost HTE effectiveness in the rotating two-pass channel [14]. The endwall average Nu_0 in the non-rotating channel was raised to 4.9–4.77 times Nu_∞ . It was highlighted that the hot spot with a local minimum Nu on a rotating surface required design precautions for cooling applications to a gas turbine rotor blade. However, this local minimum Nu in a rotating passage can only be identified after acquiring a full-field Nu map. As a result, Chang and Huang [14] identified the heat transfer rate in the worst cooling conditions for the particular rotating channel at $Ro = 0.05$ with the spotted heat transfer impairments at 0.77 and 0.82 times Nu_0 on the leading and trailing endwalls. The requirement for assessing the heat transfer margins between the averaged and minimum heat transfer levels for the internal coolant channels was highlighted [14]. While the typical Ro effects are followed by this set of heat transfer data, the Bu effect in their test range promoted local cooling performances without modifying the patterns of Nu distribution. The average Nu_0/Nu_∞ were upraised to 4.9–4.77 and the TPF values reached 1.53–1.45 and 2.39–1.48 in static and rotating conditions, respectively [14].

5.2. Rotating Non-Rectangular Channel

Considering the need to understand the cooling performance in a non-rectangular rotating channel for enhancing the design flexibility of a cooling network in a gas turbine rotor blade, the heat transfer characteristics of non-rectangular rotating channels were studied. Dutta et al. [61] studied the cooling performance of a two-pass triangular duct with two sides roughened by the transverse ribs at different channel orientations. The fully destabilized ribbed walls underwent the heat transfer elevation with Ro . Over the partially destabilized ribbed wall, the Nu/Nu_0 ratio was initially increased with Ro but was followed by a Ro -driven decreasing trend as Ro increased further. With a rotating trapezoidal ribbed channel separated by a middle plate to configure Coriolis-utilization rotating conditions, Chang et al. [39] measured the centerline Nu profiles of a rotating twin-pass trapezoidal duct with two opposite inclined walls roughened by 45° staggered ribs at two channel orientations. At Re between 5000 and 15,000, the tested Ro was controlled at 0, 0.1, 0.3, 0.5, 0.7, or 1. The isolated Ro effect improved the HTE effect over the two ribbed walls with the Bu effect to suppress their cooling effectiveness. This Bu effect was alleviated as Ro increased.

As shown in Figure 8a, the internal coolant channel of a gas turbine rotor blade often takes a parallelogram shape. However, most of the previous studies on mid-chord cooling focus on rotating rectangular channels. Chang et al. [62] compared the aerothermal

performances of two rotating parallelogram ribbed channels with and without dimples. In the channel with skewed ribs and dimples, the ribs promoted near-wall turbulent mixing by means of shedding vortices tripped in dimpled cavities. Combined with the relaxation of shear strain by enlarging channel sectionals, the Nu elevations were coupled with a minor friction factor reduction from the references in the parallelogram ribbed channel without dimples in static and rotating conditions. The augmented HTE effectiveness accounted for a minor pressure drop penalty with the addition of dimples on the ribbed surface, which resulted in TPF elevation. Liou et al. [63] reported on the heat transfer characteristics, Fanning friction factors (f), and TPFs of a radially rotating two-pass parallelogram channel with 45° ribs. The combined Re , Ro , and Bu effects on Nu and f augmentations raised the TPF values to 1.77–3.06, affirming the HTE efficiency of the continuous skewed ribs for the rotating parallelogram channel. This research group also installed transverse ribs on the leading and trailing endwalls of the rotating two-pass parallelogram channel [64]. The further HTE augmentation by the transverse ribs accompanied the boosted f/f_∞ ratios in the respective ranges of 4.6–14.7 for channel backwalls and 3–9.7 for channel sidewalls.

When a rotating rectangular/square channel is turned to a finite orientation angle, the periphery boundary that confines the development of Coriolis secondary flows are no longer rectangular. Brahim and Miloud [65] simulated the flow and heat transfer phenomena in a two-pass rotating channel enhanced by 45° ribs with two channel orientations at a reference pressure of 10-atm and an Re of 25,000. Disregarding the channel orientation angle at a low Bu , a thermal gradient between leading and trailing walls emerged in the inlet pass with radial outflow. At a high Bu , the flow interaction between Coriolis vortices, rib flows, and buoyancy-driven flow-cells were destructive to undermine the HTE effectiveness on trailing and leading walls in the inlet pass at a channel orientation angle of 0° . When the channel orientation angle is turned to 45° , the above secondary-flow interactions became constructive to promote the HTE effect on both leading and trailing walls.

5.3. Rotating Multi-Pass Channel with Variant Sectional Shapes

A serpentine coolant channel with more than three flow pathways often adjusts its sectional shape to accommodate the mid-chord blade profile. Li et al. [66] emulated the realistic two-pass coolant channel with the variant sectional shapes to explore the effect of rotation on its heat transfer performance. The inlet pass with an irregular cross-section was interconnected with the outlet pass with a nearly rectangular cross-sectioned 180° bend, giving rise to the highest Ro of 0.72 (0.37) for the inlet (exit) pass. With rotation, the ratios of the Nu/Nu_∞ were raised to 4.3 on the trailing wall in the inlet smooth pass but were not remarkably elevated on the leading wall and all sidewalls in the outlet pass. The Ro -driven Nu/Nu_0 variations exhibited different patterns at different Re , suggesting the uncoupled Re effect from the rotation is associated with flow parameters for the tested channel. This research group also investigated the effect of channel orientation on the cooling performance of the rotating ribbed channel [67] with similar channel sectional shapes. The highest Ro for the inlet (exit) pass reached 1.88 (0.972). The most remarkable Ro effect on the cooling performance emerged over the trailing ribbed wall of the inlet pass. The Nu levels were enhanced by the rotation when Ro exceeded 1 (0.5) for the entry (exit) ribbed pass.

For moderating the non-uniform Nu distribution in the sharp bend and the undesirable heat transfer reduction over the weak momentum region on the endwall downstream in a sharp bend, the channel tip-turning vane was installed in the rotating two-pass rectangular channel ($AR = 2$) with 45° ribs [68]. A stronger rotational effect was found in the tip regions compared to other endwall regions. The HTE ratio from the Dittus–Boelter reference reached four on the tip wall at $Ro = 0.42$ but was reduced to approximately 1.5 with the tip-turning vane. The tip-turning vane moderated the rotational effect, especially in the sharp bend. The authors of [69] examined the effect of the tip-turning vane on the cooling performance of the two-pass rotating rectangular channel with $AR = 4$ (2) in the inlet (exit) pass with an 180° tip turn. The profiled 60° ribs were mounted on the leading and trailing

endwalls. Owing to the different flow mean velocity and channel hydraulic diameter (D_h), the maximum Ro in the inlet and outlet passes were 0.39 and 0.16, respectively. Compared with the heat transfer results measured from the similar smooth-wall channel, the rotational effect was alleviated by ribs. There were considerable heat transfer reductions by approximately 30% over the tip wall in both the smooth and ribbed rotating channels. For the particular channel geometries, the noticeable Re effect was observed. Sahin et al. [70] considered the varying ARs from one passage to another to investigate the effect of 45° rib orientations on heat transfer in a rotating two-pass channel with an aspect ratio varying from four to two. The typical parallel (usual), reversed parallel (unusual), and crisscross 45° ribs were mounted on the inlet and outlet passes of the rotating channel. The Nu/Nu_0 ratios were decreased on the leading wall and increased on the trailing wall with Ro for the inlet pass and vice versa for the outlet pass, irrespective of the rib pattern. The overall HTE effectiveness of the usual or unusual rib patterns exceeded that of the crisscross pattern. Their follow-up work [71] installed two types of profiled V-shaped ribs on the leading and trailing endwalls of the first ($AR = 4$) and second ($AR = 1$) channels. The 45° staggered, discrete V-shaped ribs raised the Nu and TPF values from those with the traditional V-ribs and 45° ribs. The aforementioned works with the available Nu/Nu_0 and/or f/f_0 data with the corresponding tested Re , Ro , and Bu are summarized in Table 2.

Table 2. Tested conditions and heat transfer and pressure drop results of rotating coolant channels adopted for mid-chord region cooling of a gas turbine rotor blade.

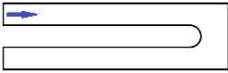
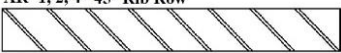
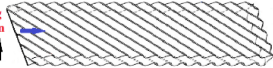
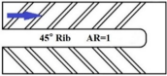


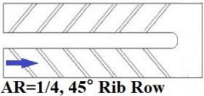
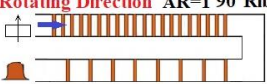
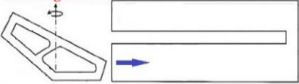
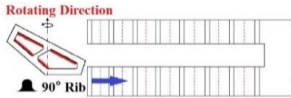
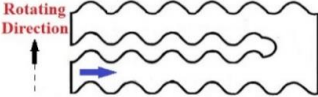



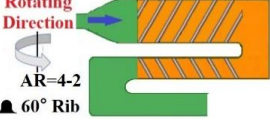
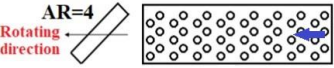
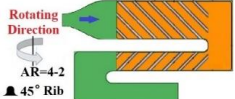
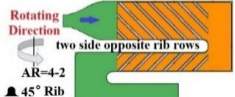
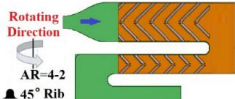
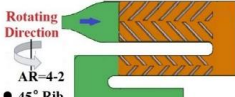
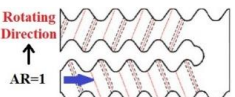
Cooling Geometry	Re	Ro	$\Delta p/\rho (\beta \Delta T)$	Bu	Nu/Nu_0	Nu_0/Nu_∞	f/f_0	f_0/f_∞	Ref.
	10,000–100,000	0–0.28	0.13–0.4	-	-	0.6–5.5	-	0.2–7.8	[41]
AR=1, 2, 4 45° Rib Row 	5000–15,000	0–2.0	0.07–0.31	0.005–8.652	0.2–1.68	2.4–2.7	-	-	[42]
Rotating Direction 	4000–14,000	0–0.22	0.03–0.09	0.003–0.11	0.77–1.46	4.08–4.23	-	-	[46]
	4000–16,000	0–0.8	0.05–0.1	0.0015–0.93	0.7–2.3	3.1–4.9	-	-	[6]
	5000–12,500	0–0.6	0.07–0.3	0.0021–0.863	0.7–3.3	3.2–3.8	-	-	[57]
Rotating Direction AR=2 	5000–15,000	0–0.3	0.06–0.188	0–0.23	0.74–2.4	3.44–6.71	0.6–5.7	3	[62]
	4000–10,000	0–0.4	0.042–0.14	0.0016–0.24	0.76–1.91	2.94–3.78	-	-	[63]
Rotating Direction AR=1 90° Rib 	20,000–50,000	0–0.8	-	0–1.8	0.75–1.55	2–3.6	-	5.5–10.5	[48]
Rotating Direction 	25,000–50,000	0–0.72	0.138	0–1.31	0.75–2.5	1.85–1.95	-	-	[66]

Table 2. Cont.

Cooling Geometry	Re	Ro	$\Delta\rho/\rho$ ($\beta\Delta T$)	Bu	Nu/Nu_0	Nu_0/Nu_∞	f/f_0	f_0/f_∞	Ref.
	10,000–50,000	0–1.88	0.138	0–9.02	0.8–5	2.7–2.9	-	-	[67]
	5000–15,000	0–0.5	0.03–0.12	0–0.15	0.93–2.34	-	1.21–2.04	-	[59]
	5000–20,000	0–0.3	0.0263–0.119	0.0015–0.122	0.68–2.16	-	0.9–2.8	-	[64]
	10,000–40,000	0–0.42	-	-	0.65–1.55	3.5–5.7	-	-	[68]
					0.87–1.3	3.75–5.4	-	-	
	10,000–70,000	0–0.39	-	-	0.68–1.4	2.5–4.2	-	-	[69]
	5500–25,000	0–1.24	0.05–0.11	0–3.86	0.6–1.45	1.8–5.7	-	-	[58]
	10,000–70,000	0–0.39	-	-	0.6–1.65	2.3–4.5	-	-	[70]
					0.5–1.3	2–4	-	-	
	10,000–45,000	0–0.39	-	-	0.75–1.8	3–4.9	-	-	[71]
					0.45–1.9	2.8–5	-	-	
	5000–15,000	0–0.4	0.058–0.14	0–0.183	0.7–2.2	3.98–5.34	0.9–1.8	32–35	[14]

In Table 2, the attainable laboratory conditions in terms of maximum $\Delta\rho/\rho$ ($\beta\Delta T$), Re , Ro , and Bu for the rotating channels with ribs, dimples, and/or wavy walls were in the respective ranges of 0–0.3 [42], 4000 [63]–70,000 [69,70], 0–2 [42], and 0–9.02 [67]. The corresponding ranges of Nu_0/Nu_∞ and Nu/Nu_0 for the enhanced channel walls reached

1.8 [58]–6.71 [62] and 0.2 [42]–3.3 [47]. The reported Re and Ro reached realistic engine conditions, yet the current density ratios ($\Delta\rho/\rho = \beta\Delta T$) tested were far less than the real engine condition. In general, the Nu_0/Nu_∞ ratios [58] were lower than those with the skewed ribs, while the combination of 45° ribs and dimples [62] boosted the Nu_0/Nu_∞ ratio to 6.71 at $Re = 5000$. The compound HTE measure in an internal coolant channel of a gas turbine rotor blade amplifies the cooling effectiveness, which is worthy of future study.

The cooling performances in the rotating channels applicable to the mid-chord cooling of a gas turbine rotor blade varied with channel shape (orientation) and the HTE elements (methods). In the literature, the full Nu maps over the rotating surfaces involving Bu effects are relatively rare in comparison with the heat transfer data detected from thermocouple measurements. As it is more critical to identify the minimum Nu on a rotating surface for preventing material burnout, the correlative analyses between the regionally minimum and averaged Nu for a variety of rotating channels should take priority in order to characterize the safety margin when an internal cooling design of a gas turbine rotor blade is relied on for the heat transfer data to be converted from thermocouple measurements. In the previously reviewed works for mid-chord cooling, the available Nu/Nu_0 data against Ro are summarized in what follows to comparatively reveal the differential Ro effects caused by channel shape, HTE elements between ribs and dimples, and the various types of HTE attempts.

The aforementioned channel-shape effect on the cooling performance of a rotating passage is closely relevant to the structure of the Coriolis vortices on the sectional plane, which is confined by the solid boundary shaped by a rotating channel. Figure 9a exhibits the conceptual flow structures induced by rotation and/or ribs on the sectional planes of the channels with various shapes. As illustrated previously, the structures of the Coriolis vortices vary with the shape and orientation of the rotating channels. The directions of these Coriolis vortices are reversed between the rotating channels with radial outflow and inflow. The flow cells tripped by the angled ribs are orthogonal to the Coriolis vortices with their structures altered by the arrangements and configurations of the angled ribs. Due to such orthogonality between the secondary flows induced by rotation and endwall ribs, a particular channel shape is in favor of the development of either Coriolis vortices or rib-induced flow-cells, leading to the respective dominance of Ro or rib configuration on its Nu/Nu_0 characteristics. Using the in-lined continuous angle rib as an illustrative example in Figure 9a, the swirling directions of these rib-induced flow cells in the rotating rectangular channels with different ARs are reversed when the rib orientation is switched from a positive to a negative angle. A rich mode of vortical interactions between the Coriolis vortices and the rib-induced flow cells is accordingly developed due to the different flow structures of Coriolis vortices and the rib-induced flow cells. In this respect, the channel orientation and shape, including different ARs for rectangular channels, the positive/negative rib angles, the rib arrangement (staggered and in-lined arrangements), the rib configurations, and the direction of the bulk coolant stream (radial inflow and outflow) are the geometric factors affecting the cooling performance of a rotating channel. The cooling impacts caused by these geometric factors were extensively studied [3–6,13,39–53,61–80]. Another study utilized the alternative HTE methods, including dimples, impinging jets, and wavy endwalls or sidewalls, to investigate their effects on the cooling performances of the rotating channels.

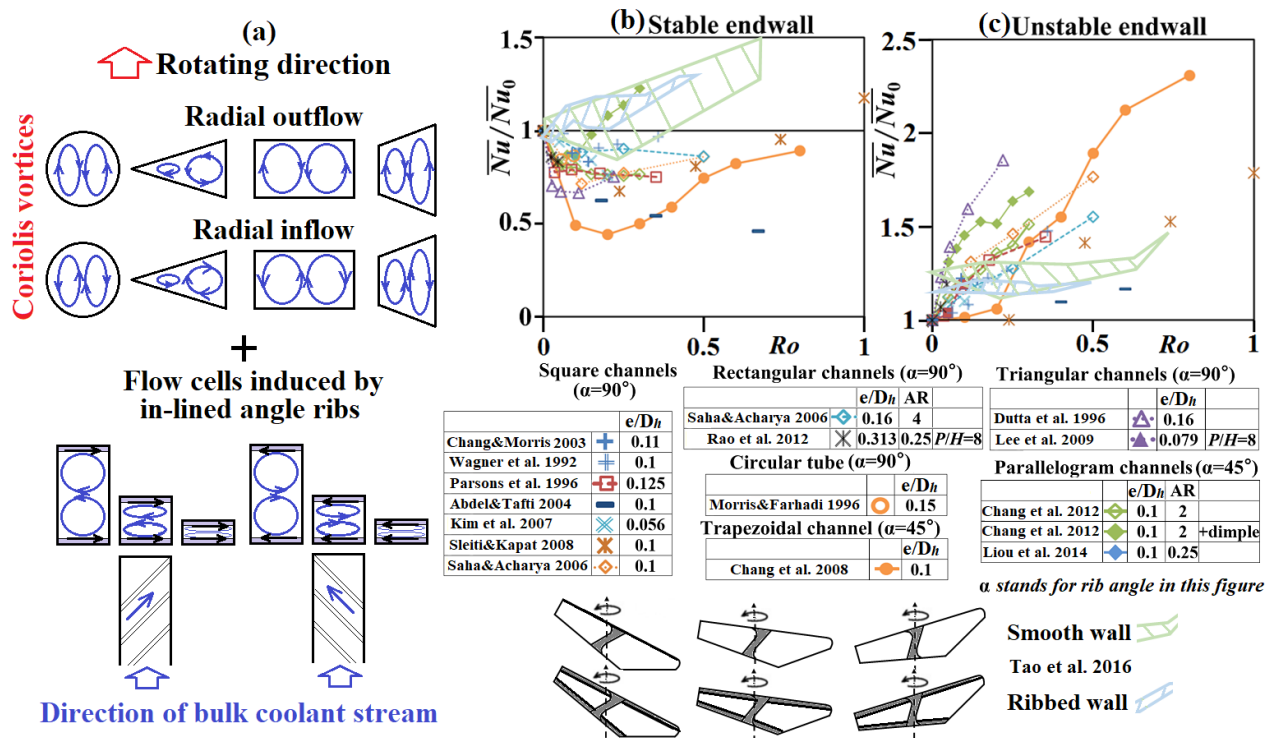


Figure 9. (a) conceptual flow structures on the cross-section of a rotating ribbed coolant channel; variations of endwall-averaged Nu/Nu_0 ratio against Ro on (b) stable (c) unstable walls of the rotating ribbed channels with square, circular, trapezoidal, triangular, and parallelogram shapes [2,4,20,61–63,72–80].

In Figure 9b,c, the variations of the endwall-averaged Nu/Nu_0 ratio against Ro on the stable and unstable walls of the rotating ribbed channels with square, circular, trapezoidal, triangular, parallelogram, and irregular (realistic) shapes are compared. The heat transfer data reported in the literature [2,4,20,61,63,67,72–80] exhibited a common trend of Ro -driven variations on the stable or unstable channel wall with different Nu/Nu_0 ratios. In Figure 9b, the Nu/Nu_0 ratios on the stable wall are initially reduced from unity (static-channel reference) and then recovered to be increased with Ro as Ro increases from zero to one. However, the critical Ro , above which the Nu/Nu_0 ratio was turned to be increased with Ro , varies with channel sectional shape, rib configurations, and thermal boundary conditions. With Ro in the range of 0.1–0.2, the Nu/Nu_0 ratios among the comparative group with different channel shapes in Figure 9b range from 0.5 to 1.02 and require design precautions to avoid overheating spots on the stable wall of a rotating channel. In Figure 9b, the severe heat transfer impediments with the lowest Nu/Nu_0 ratio less than 0.5 developed in the rotating trapezoidal channel with angled ribs. Over the unstable wall in Figure 9c, all the Nu/Nu_0 ratios the range of 1–2.3 keep increasing with Ro disregarding the sectional shape of the rotating channels. Furthermore, a systematic study aimed at identifying the critical Ro with typical (but realistic) channel configurations is beneficial for designers to parametrically plan the operating conditions of the internal cooling schemes. With the realistic channel shapes for the two-pass smooth and ribbed rotating channels [67], the degrees of heat transfer impediments on the stabilized smooth and ribbed walls in Figure 9b, as well as the heat transfer elevations on the destabilized smooth and ribbed walls in Figure 9c, are not as significant as those generated in the circular, square, rectangular, trapezoidal, and parallelogram channels. The Ro effects on the cooling performances in the rotating two-pass channels with various channel shapes for the inlet and exit passes [67] are comparatively alleviated.

In the coolant channels over the mid-chord region of a gas turbine rotor blade, the ribs and dimples are the most common HTE elements. Figure 10 compares the variations of the Nu/Nu_0 ratio against Ro on the rotating, leading, and trailing walls of the rectangular

channel ($AR = 4$) with 45° ribs [42], the rectangular channel ($AR = 2$) with hemispherical protrusions [57], the rectangular channel ($AR = 4$) with dimples [58], and the parallelogram channel ($AR = 2$) with 45° ribs and dimples [62]. The bulk coolant stream in these rotating single-pass channels [42,57,58,62] flow in a radially outward direction. Between the rotating rectangular channels ($AR = 4$) enhanced by the 45° ribs [42] and dimples with effusion [58] as compared in Figure 10, the Nu/Nu_0 ratios on the leading (trailing) wall of the rotating ribbed channel [42] are lower (higher) than their dimpled-channel counterparts [58]. The Ro effects which incurred the respective heat transfer impediments and enhancements on the leading and trailing walls of the rotating ribbed channel were stronger than those in the dimpled channel [58]. While the employment of hemispherical protrusions in the rotating rectangular channel [57] advances the critical Ro from that with the concave dimples [58] to a lower value, which comparatively boosts their Nu/Nu_0 levels on both leading and trailing walls from their dimpled-channel counterparts in Figure 10, the compound HTE measure with 45° ribs and dimples in the rotating parallelogram channel [62] can further promote the Nu/Nu_0 ratios from those elevated by the hemispherical protrusions [57]. The compound HTE methods involving ribs and concave/convex dimples for promoting the cooling performance of a rotating channel is worthy of future study.

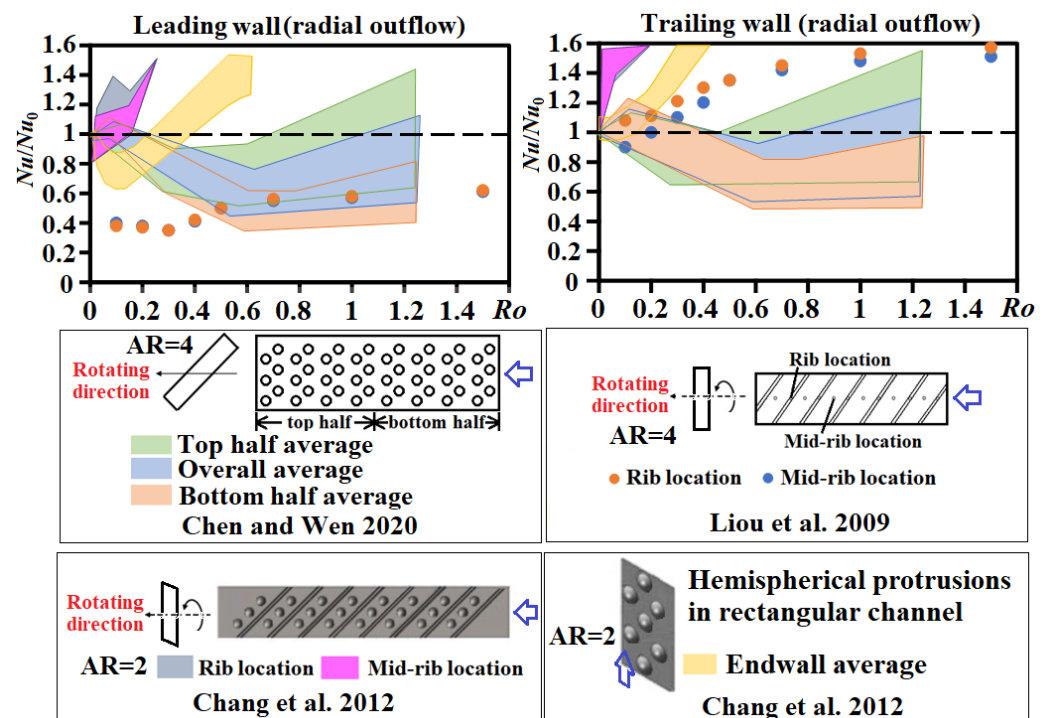


Figure 10. Variations of Nu/Nu_0 against Ro on rotating, leading, and trailing walls of rectangular channel ($AR = 4$) with 45° ribs [42], rectangular channel ($AR = 2$) with hemispherical protrusions [57], rectangular channel ($AR = 4$) with dimples [58], and the parallelogram channel ($AR = 2$) with 45° ribs and dimples [62].

6. Trailing-Edge Cooling

In the trailing edge of a gas turbine rotor blade, the blade profile significantly limits the shape of its internal coolant passage. Accordingly, narrow rectangular, wedge-shaped, or triangular channels are commonly embedded in the tail end of a turbine rotor blade. The endurance of thermal and mechanical loads by the slim airfoil tail with the HTE element of a pin-fin array in the coolant channel can also enhance its structure integrity. In this respect, a pin fin array has become the most popular HTE device for the coolant channel in the trailing-edge region of a gas turbine rotor blade. Du et al. [8] reviewed the state-of-art cooling arrangement, which considered the airfoil aerodynamic efficiency, structure/strength of

the blade, and the manufacturing availability, in the trailing edge of gas turbine blades. The correlative analysis between the flow structure and heat transfer characteristics for the trailing-edge rotating channels with pin fins, latticework, dimples/protrusions, and/or labyrinth passages were emphasized in the review. In the literature, the aerothermal performances of the rotating trailing-edge coolant channels with smooth walls, pin fins, dimples, and lattice works were studied.

6.1. Smooth-Walled Channel

Wright et al. [81] measured the regionally averaged Nusselt numbers in a wedge-shaped channel with Re , Ro , and Bu in the respective ranges of 10,000–40,000, 0–1.0, and 0–3.5. The spanwise (streamwise) Nu variations on the smooth rotating walls were mainly attributed to the wedge-shaped channel (the sharp entrance and 180° bend). By changing the channel orientation from 0° to 135°, the Nu levels on all rotating walls were increased.

Li et al. [82] proposed a two-inlet, wedge-shaped channel with side-wall ejection for trailing-edge cooling of a gas turbine rotor blade. The mass flow ratio (MR) between the sidewall injection at the channel tip region and the main radial outflow varied from zero to one. The two-inlet inflow promoted (undermined) the local cooling performance over the top-half (bottom-half) endwall portion at $Ro = 0$. In the rotating channel, the increase in the MR moderated the trailing-to-leading Nu difference due to the two-inlet inflow. This research group also examined the cooling performance of a rotating two-inlet inflow rectangular channel ($AR = 4$) at an orientation angle of 135° with the MR varying from 0–0.6 [83]. When the MR exceeded a critical value, the Nusselt numbers on the leading wall of the rotating channel were higher than those on the trailing wall. A higher critical MR in the rotating channel was found owing to the suppressed radial inflow by rotation. For the wedge-shaped, two-inlet, smooth-walled channel, the sidewall coolant injection at the channel tip provided the optimal cooling performance in static and rotating conditions [84]. When the eight lateral coolant injections were distributed with an equal interval along the supplementary inflow channels at Ro up to 1.1 [85], the increase in the MR promoted (weakened) cooling effectiveness over the top-half (bottom-half) endwall regions. With an $MR > 0.5$, the Ro -induced overall heat transfer variations became less than 6%.

6.2. Pin Fin Channel

Chang et al. [86] measured the centerline Nu profiles on the leading and trailing walls of a radially rotating pin fin channel at Ro in the range of 0–1.4. While the Nu on the trailing endwall kept increasing with Ro , the leading Nu was initially reduced from Nu_0 as Ro increased from 0 to 0.1, above which the Nu level turned to increase with Ro . With the Coriolis forces directing toward the trailing wall, the pin fin tripped vortices were attached firmly on the trailing wall but lifted from the leading wall to incur the trailing-to-leading Nu reduction at each measured channel section. The worst cooling conditions of the rotating channel emerged on the leading wall with the minimum Nu/Nu_0 ratios down to 0.89 and 0.8 at the locations behind and in front of the pin row, respectively. Park et al. [87] used the naphthalene sublimation technique to detect the endwall heat/mass transfer maps for the rotating rectangular channel with inclined pin fins at Ro up to 0.2. It was concluded that the inclined pin fin array from the vertical orientation to a channel wall always deteriorated its heat/mass transfer effectiveness, which was approximately 15% at the inclined angle of 60° in both stationary and rotating conditions. While the rotation levels at $Ro = 0.2$ exhibited a limited rotational effect, the rotation generally rendered an overall Nu elevation from Nu_0 . Chang et al. [88] measured the endwall Nu maps on leading and trailing walls of a rotating rectangular channel enhanced by the diamond-shaped pin fin array with radial outflow at Ro and Bu in the respective ranges of 0–0.6 and 0–0.31. The combined Ro and Bu effects qualitatively followed the typical results for a rotating single-pass channel that resulted in the average Nu/Nu_0 ratios on the leading (trailing) endwall to the ranges of 0.82–1.52 (1–1.89). In comparison with the heat transfer data generated from the similar rotating channel with circular pin fins, the isolated Ro effect on the leading Nu/Nu_0 ratios

with the circular and diamond-shaped pin fins remained similar but exhibited a lesser degree of HTE benefits compared with the Coriolis force effects on the trailing wall in the rotating channel with diamond-shaped pin fins. As a pin fin array in a channel considerably disrupted the development of the sectional vortices to alleviate the fluid mixings, Chang and Hu [19] extend the rib land to permit the embodiment of a pin row with a skewed rib. The interaction between the rib-induced vortical flows and the vortex system tripped by the pin fins generated a high Nu_0 ring around the slender pin fin that superimposed on the Nu_0 map with rib-wise heat transfer decay to signify its endwall heat transfer characteristic. The ratios of Nu_0/Nu_∞ reached 6.1–5 with $5000 \leq Re \leq 15,000$. The isolated Coriolis force effects at $Ro \leq 0.4$ led the leading (trailing) Nu/Nu_0 ratios to become 0.93–1.23 (1–1.28) with the Bu effect to promote the local cooling effectiveness on both leading and trailing endwalls.

Huang et al. [89] adopted the liquid crystal and stroboscopic method to measure the Nu map on the leading and trailing endwalls of the rotating rectangular channel ($AR = 4$) with the staggered or inline pin fin array at $5000 \leq Re \leq 20,000$ and $0 \leq Ro \leq 0.52$. Without rotation, the overall heat transfer rate promoted by the staggered array was 25–30% higher than that of the inline pin fin array. The overall heat transfer enhancements caused by rotation were 22% and 93% for the staggered and inline pin fin arrays, respectively, suggesting the secondary flows induced by the pin fin played a dominant role for the staggered array. Liu group [90] subsequently examined the effect of channel orientation on the cooling performance of the rotating rectangular pin fin channel. At the channel orientation angle of 150° , a larger spanwise Nu variation was resolved due to the deformed Coriolis vortices. At the channel orientation angle of 90° , the inline pin fin array generated the largest Ro -induced HTE effect. When the staggered pin fin array was composed by the non-uniform sizes of circular pins at a channel orientation of 135° [91], the higher local fluid velocities through the fin spaces among the pin fin array composed by the large sized pins promoted local convective flow and hence local Nu . Furthermore, the friction factor increased with the size of the pin fins.

Du et al. [92] numerically examined the heat transfer and flow characteristics in a single-pass rotating rectangular pin fin channel with different dimple locations. Behind the pin row, a counter-rotating vortex was induced by the Coriolis force to convect wakes from trailing-to-leading endwalls. By shifting dimples close to the leading edge of pin rows, the endwall Nu were increased. While the trailing Nu was consistently higher than the leading counterpart, the average Nu on both leading and trailing walls were increased with Ro . Luo et al. [93] numerically explored the effects of convergence angle and dimple shape on the flow structure and cooling performance of a wedge-shaped rotating pin fin channel. The cooling performance of the dimple-pin wedge channel with radial outflow was improved by Ro and/or by increasing its convergence. With a converging angle of 12.7° , the strong downwash flow squeezed by its opposite converging endwall elevated the leading-wall Nu from that of the trailing dimpled endwall. With such strong downwash flow, the Coriolis force effect was alleviated. The amplified turbulent kinetic energy in the vicinity of the dimple with the stronger vortex tripped by the spanwise-elliptical dimples generated a higher HTE effectiveness. Li et al. [94] investigated the combined effect of two inlets and pin fins on the cooling performance of a rotating wedge-shaped channel with radial outflow. With rotation and MR above a critical ratio, the Ro effect was diminished so that the Ro effect was suppressed by the lateral entry flow stream. At a low MR with the radial outflow to dominate the cooling performance of the rotating channel, the heat transfer rate at a channel orientation angle of 135° was less than that at 90° . For such two-inlet rotating pin fin channels, the Ro effect on average heat transfer properties was sensitive to channel orientation rather than the channel shape or pin fins.

Liang and Rao [95] numerically studied the effect of pin fin compositions, which involved detached pins, on flow and heat transfer characteristics of a static and rotating rectangular channel at $Ro = 0.15$. With detached pins in a pin fin array, the flow above the top face of each detached pin generated the additional transverse vortices in the wake zone behind the pin to promote the local heat transfer rate on the endwall behind the detached

pin and improve heat transfer uniformity. With the reduced (increased) friction factors (overall Nu) by 31.9% (16.9%), the thermal performance parameters were raised up to 29.1% compared to those with full-height pin fins. Yan et al. [96] comparatively examined the HTE effectiveness of upright/curved/inclined pin fins in the rectangular channel ($AR = 0.7$) with Ro varying from 0 to 0.5. With rotation, the HTE performance with the curved pin fins was insensitivity to Ro compared to the other two types of pin fins. On the trailing wall of the rotating channel, a strong pressure gradient close to the pin induced the longitudinal secondary flows behind pin fins to elevate the Nu/Nu_0 ratio, which was increased with Ro .

Madhavan et al. [97] measured the Nu maps on the leading and trailing walls of a rotating coolant channel that covered both the mid-chord region and trailing edge of a gas turbine rotor blade. The coolant after entering the 2:1 rectangular ribbed channel was reformed into the crossover jets into the 4:1 trapezoidal pin fin channel with lateral discharge. The lateral jet impingement into the pin fin array promoted fluid mixings in the trailing-edge coolant channel. At $Ro = 0.1$, the channel-averaged Nu on trailing was approximately 28% and 7.6% higher than their leading counterpart in the ribbed and pin fin passes, respectively. Liang et al. [98] carried out an experimental and numerical study to explore the flow and heat transfer characteristics in a rotating wedge-shaped channel with the innovative guiding pin fin arrays. The endwall-averaged Nu promoted by the guiding pin fin arrays was approximately 33.7% (23%) higher than those with a circular pin fin array in static (rotating) conditions. With the guiding pin fin arrays at $Ro = 0.46$, the trailing-to-leading Nu difference was considerably alleviated from those with a circular pin fin array, leading to improved heat transfer uniformity. Zhang et al. [99] examined the heat transfer characteristics in a rotating trapezoidal pin fin channel with lateral flow exits at Re and Ro in the respective ranges of 10,000–110,000 and 0–0.5. At a fixed Ro with different rotating speeds, the heat transfer results at a high Re were similar to those at a low Re . The critical Ro above which the Nu/Nu_0 on the leading wall turned to be increased with Ro varied with the radial location in the rotating pin fin channel.

6.3. Dimpled Channel

Jing et al. [100] numerically examined the effects of Ro , dimple arrangement, and channel orientation on the flow and heat transfer characteristics of rotating trapezoidal channels with lateral coolant discharge. The cooling performance of the rotating wedge-shaped channel was considerably improved by dimples. A maximum 108.2% Nu improvement on the trailing wall of the rotating dimpled channel was achieved by increasing Ro . Chen et al. [101] experimentally explored the heat transfer characteristics of a rotating trailing-edge coolant channel with pin fins and dimples at Re , Ro , and Bu in the respective ranges of 12,000–20,000, 0–0.89, and 0–1.32. The high HTE region on the tip region of the endwall was contracted by rotation. The endwall subjected to heat transfer reduction was expanded in radially inward direction with Ro . The Bu effect impaired (promoted) heat transfer rates at low (high) Ro . In view of the coupled and isolated Ro and Bu effects, the governing dimensionless flow parameters evaluated at local values were more instructive than those defined by flow entry conditions.

6.4. Latticework Channel

Oh et al. [102] investigated the heat/mass transfer and pressure drop characteristics in a matrix cooling channel at Ro in the range of 0–0.8. The flow complexities induced in the static matrix channel raised the endwall average heat/mass transfer rates to approximately 2.1 times greater than those in a likewise smooth channel. As Ro increased, the Sherwood number ratios on the leading wall also increased but altered slightly on the trailing wall, whereas the f/f_0 ratios decreased with Ro , leading to increased thermal performance factors. Du et al. [103] numerically examined the effect of broken rib locations on the flow and heat transfer characteristics of a rotating latticework channel with radial outflow. The flow characteristic was dominant by the induced upward spiral and helical flows among the lattice maze with local flow impingement induced by the upward spiral flow to promote

local heat transfer rate and wall shear stress. Using the broken skew ribs to configure the latticework, the average Nu was elevated by 6.12% (6.02%) on the trailing (ribbed) endwall compared to those with conventional latticework. The Nu/Nu_0 ratio was decreased with Ro by up to 5.4% over the trailing (pressure) wall. Heat transfer elevations on the leading (suction) wall emerged at high Ro at which the friction factors were reduced, leading to an increase in the thermal performance factor by 12.12% using the broken ribs.

The studies with the available Nu/Nu_0 and/or f/f_0 data for the trailing-edge cooling of a gas turbine rotor blade at the tested Re , Ro , and Bu are summarized in Table 3. The rotating wedge-shaped channels and rectangular channels with large ARs are mostly adopted. While the heat transfer performances of the rotating pin fin channels are extensively studied, the high Nu_0/Nu_∞ ratios achieved by the compound pin fins with angle-ribs [19] and the latticework composed by the skewed broken ribs [103] are worthy of future study.

Table 3. Tested conditions and heat transfer and pressure drop results of rotating coolant channels adopted for trailing-edge cooling of a gas turbine rotor blade.

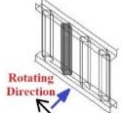

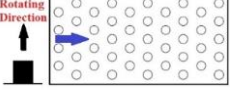
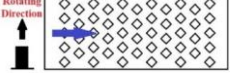
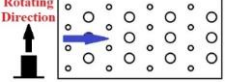
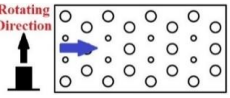
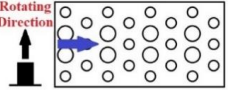
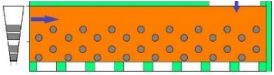
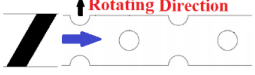

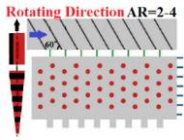
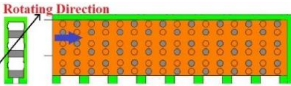
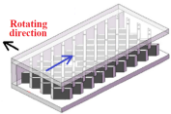
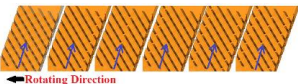
Cooling Geometry	Re	Ro	$\Delta p/\rho (\beta \Delta T)$	Bu	Nu/Nu_0	Nu_0/Nu_∞	f/f_0	f_0/f_∞	Ref.
	5000–15,000	0–0.4	0.08–0.18	0.0007–0.31	0.94–1.43	5–6.1	0.43–0.99	-	[19]
	10,000–25,000	0–1.06	-	0–3.2	0.9–2.9	1.8–5.3	-	-	[82]
	5000–20,000	0–1.4	0.1–0.24	0.004–3.6	0.79–2.47	2.3–3.1	-	-	[86]
	5000–15,000	0–0.6	0.0032–0.1519	0–0.31	0.82–1.89	2.21–2.77	-	-	[88]
					0.95–1.1	1.95–2.4			
	10,000–20,000	0–0.33	-	-	0.05–1.075	1.9–2.45	-	-	[91]
					0.93–1.2	1.9–2.55			
	20,000–45,000	0–0.155	-	0–0.075	0.72–1.25	1.6–9	-	-	[94]
					0.812–1.432	1.75–2.65			
	7000–18,600	0–0.5	-	-	0.99–1.31	2–2.5	-	-	[96]

Table 3. Cont.

Cooling Geometry	Re	Ro	$\Delta\rho/\rho$ ($\beta\Delta T$)	Bu	Nu/Nu_0	Nu_0/Nu_∞	f/f_0	f_0/f_∞	Ref.
	20,000	0–0.14	-	-	2.1–3.5	2.25–3.7	-	-	[97]
	12,000–20,000	0–0.89	0.05–0.1	0–1.32	0.56–1.05	1.5–10.1	-	-	[101]
	10,500–44,000	0–0.8	-	-	0.9–1.18	1.5–4.8	-	-	[102]
	44,000	0–0.5	-	-	0.961–1.07	4.58–4.92	-	350–460	[103]

With the application of trailing-edge cooling of a gas turbine rotor blade, the variations of Nu/Nu_0 ratios against Ro for the rotating rectangular channel with the compound pin fins and angle ribs [19], wedge-shaped smooth channel [81], two-inlet, wedge-shaped smooth channels [82–85], rectangular [86,88–91,96], wedge-shaped [99], and wedge-shaped two-inlet [94], pin fin channels, wedge-shaped channel with dimples [100], rectangular channel with compound dimples and pin fins [101], and rectangular latticework channels [102,103] are summarized in Figure 11 for (a) leading (stabilized) and (b) trailing (destabilized) walls.

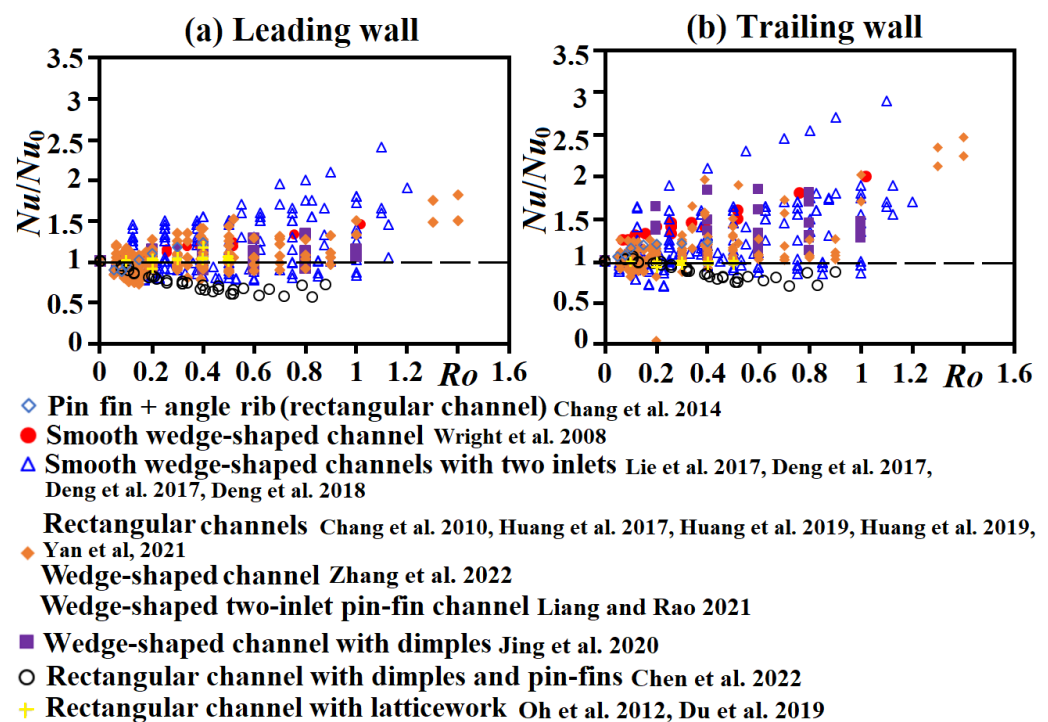


Figure 11. Variations of Nu/Nu_0 with Ro on (a) leading and (b) trailing walls of the rotating channels typical in the trailing edge of a gas turbine rotor blade [19,81–86,89–91,94,96,99–103].

In Figure 11, the Nu/Nu_0 ratios on the trailing walls of all rotating channels are higher than their leading-wall counterparts, irrespective of the channel shape, channel orientation,

and HTE type. As Ro increases, the leading-wall Nu/Nu_0 ratios are initially reduced and then increased after Ro exceeds the critical values (Ro_{cr}). Owing to the channel orientation effect that shifts the trailing wall of a rotating channel from the typical un-stabilized (trailing) wall at an orientation angle of zero degree, some of the trailing-wall Nu/Nu_0 ratios for the rotating channels with the orientation angles of approximately 135° in Figure 11b are less than unity. The enhanced fluid-mixing effects by using the two-inlet, wedge-shaped channel cause a large data spread in Figure 11a,b due to the interdependent Re and Ro effect on Nu/Nu_0 . For rotating channels with compound pin fins and angle ribs [19] or dimples [101], the range of Nu/Nu_0 variation caused by varying Ro are generally less than the other comparative groups in Figure 11. Particularly, with the maze-like shallow flow passage in a channel with latticework to prohibit the development of Coriolis vortices on the sectional plane, the Nu/Nu_0 ratios become insensitive to Ro , which are scattering around unity in Figure 11a,b. The Coriolis force effects are significantly suppressed in a rotating latticework duct.

7. Prospective Works

7.1. Realistic Engine Conditions

Previous cooling studies for gas turbine rotor blades [1–103] attempted to emulate the realistic operating conditions in terms of Re , Ro , Bu , and the geometric features to devise novel HTE methods for improving aerothermal performances by augmenting HTE effectiveness, reducing non-uniformity of Nu distribution, and/or alleviating pressure drop penalties. Engine development urges continuous advancements in this research area to devise more effective and efficient HTE elements applicable to internal cooling schemes in a gas turbine rotor blade. A special need in this regard is to generate the heat transfer data with realistic density ratios ($\beta(T_w - T_f)$) in the range of approximately 1.1–1.7 [1]. Considering typical engine conditions and a mid-span eccentricity of 250–350 mm and a coolant channel effective diameter of approximately 3–7 mm at $Ro = 0.3$ for a commercial gas turbine engine at a rotor speed of 5000–20,000 rev/min and density ratio ($\Delta\rho/\rho = \beta\Delta T$) of 1.1–1.7, the corresponding Bu reaches 4.95–17.85, which is far beyond the laboratory test conditions summarized in Tables 1–3. The novelty in experimental method for acquiring the heat transfer data at the realistic Bu range should be prioritized.

From the viewpoint of avoiding hot spots in a gas turbine rotor blade, the coolant temperature and the internal (external) heat transfer rates of coolant (gas) flow are both crucial. After a long journey of coolant flowing through a multi-pass channel, the coolant and material temperatures of a gas turbine blade are raised in a downstream direction owing to the enthalpy increase in the cooling flow. The effect of this coolant temperature increase on material temperature elevation is not visible from the Nu result. Yet, the dimensionless wall temperature (η_w) involved in Equation (13), hence a η_w map over a rotating surface, is capable of reflecting both variations in Nu and coolant temperature. The reference temperature for normalizing the energy conservation in Equation (13), namely the fluid temperature increase (ΔT_f) through a rotating coolant passage, can be calculated by Equation (17),

$$\Delta T_f = Q / (\dot{m} \times C_p) \quad (17)$$

the local value of $(\eta_w - \eta_f)$ is inversely proportional to $Nu/(RePr)$ as η_w (η_f) takes the dimensionless form of:

$$\eta_w(\eta_f) = T_w(T_f) / \Delta T_f \quad (18)$$

In Equations (17) and (18), the definition of ΔT_f is based on the thermal power (Q) transferred into a gas turbine rotor blade from its surrounding hot gas and the specific heat of the coolant (C_p), which are generally prescribed at a design stage for its internal cooling system. Figure 12 depicts the full-field distributions of (a,d) endwall temperature (T_w), (b,e) dimensionless wall-to-fluid temperature difference ($\eta_w - \eta_f$), and (c,f) convective heat transfer coefficient (h) evaluated at the local fluid bulk temperature for a static triple-pass ribbed and pin fin channel with internal effusion [104]. In Figure 12a,d, each T_w map

reflects the combined effect of the spatial h variation and the streamwise increase in the fluid bulk temperature along the cooling passage. As compared in Figure 12c,f, the endwall h values over the tip region on the third-pass pin fin endwall are significantly elevated by the near-wall effusion flows. However, the wall temperatures over this corresponding endwall region in the third-pass pin fin channel in Figure 12a,d are still raised due to the increased fluid bulk temperature after the coolant travels through the first smooth and the second ribbed passages. The $(\eta_w - \eta_f)$ maps in Figure 12b,e can truly reflect the combined effects of increased fluid bulk temperature and the h variations along these flow pathways. Following Equation (14) that formulates the cooling research strategy for gas turbine rotor blades, η_w can also be parametrically defined as Equation (19) to include the streamwise increase in local fluid temperature (η_f):

$$\eta_w = \Phi\{Re, Ro, Bu, Pr, \eta_f, \text{boundary conditions}\} \quad (19)$$

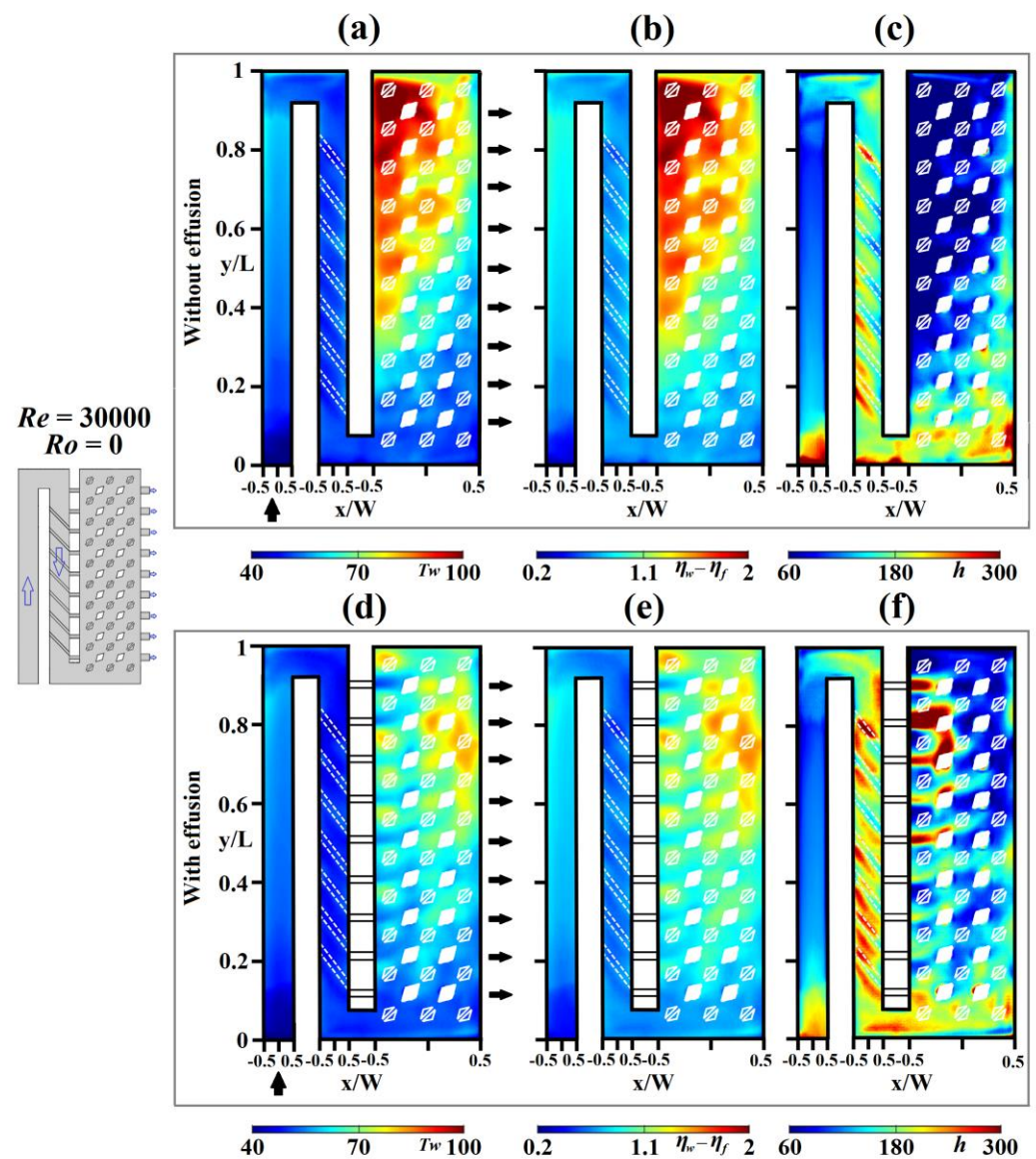


Figure 12. Full-field distributions of (a,d) endwall temperature (T_w), (b,e) dimensionless wall-to-fluid temperature difference ($\eta_w - \eta_f$), and (c,f) convective heat transfer coefficient (h) evaluated at the local fluid bulk temperature for a static triple-pass channel with internal effusion. (Reprinted/adapted with permission from Ref. [104]. 2022, copyright Elsevier.)

For enhancing the industrial and academic research links, the analysis and presentation of a set of heat transfer data in terms of $(\eta_w - \eta_f)$ is recommended, especially for the multi-pass coolant channel in a gas turbine rotor blade.

7.2. Hot Spot Prevention

In addition to the continuing endeavors aimed at improving the aerothermal performances of the rotating coolant passages in a gas turbine rotor blade using a variety of HTE measures, a noteworthy approach for preventing hot spot development in a gas turbine rotor blade is the direct mixing of cold and hot coolant using the supplementary supply of the cold coolant stream from a two-inlet channel [82–85] or the internal effusion as exemplified by Figure 12. An adequate internal effusion scheme not only alters the flow structure in a way that promotes local heat convection, but also reduces the fluid temperature when a cold stream extracted from the upstream flow region is mixed with the downstream hotter coolant [104]. However, relevant heat transfer studies considering a rotating channel with internal effusion are lacking.

While novel cooling methods applicable to a gas turbine rotor blade pursue the heat transfer elevations which are Re -, Ro -, and/or Bu -dependent for a particular channel configuration [1–103], a designer is keen to avoid the cooling network running at the worst operating scenarios in which the combination of Re , Ro , and/or Bu give rise to the minimum Nu/Nu_0 ratios. In this design respect, the hydraulic diameter of a coolant channel, which affects Re , Ro , and Bu at a set of prescribed coolant mass flow rates, rotor speeds, and thermal and geometric constraints, is adjustable to permit the Re , Ro , and/or Bu of the coolant flow in a rotating channel away from the worst heat transfer scenarios. This design initiative requires a researcher to report the worst heat transfer conditions for a particular cooling flow configuration. In general, the minimum Nu/Nu_0 often emerges at the critical Ro on a rotating stabilized surface. In [86], the parametric analysis of the endwall average Nu/Nu_0 ratios against Ro and Bu revealed that the critical Ro varied with Bu for the rotating pin fin channel at high Ro . Along with the results of $(\eta_w - \eta_f)$, Nu , and f , the exploration of the minimum heat transfer levels aimed at determining the critical Ro and Bu for a particular cooling flow configuration is advantageous for preventing hot spot development by a designer.

Above all, advancements in experimental methods and CFD tools enable researchers to explore the aerothermal performances of rotating coolant channels in conditions closer to realistic engine conditions with more complicated channels and HTE geometries. However, most of the previous studies measured the local or regional average Nu instead of a full-field Nu map for a rotating coolant channel. With complex flow structures in a rotating channel, the local and regional average Nu data often deviate from the minimum Nu on a rotating surface. The discrepancies between the local-minimum and regional-average Nu can be evaluated from the Nu maps of rotating surfaces, which are beneficial for a designer to justify the usage of the vast local heat transfer data in the literature. Meanwhile, the full Nu map involving Re , Ro , and Bu effects for a rotating coolant channel in realistic engine conditions should be prioritized, as a critical Ro can be Bu -dependent [86]. The identification of the levels and locations of the local minimum Nu in a rotating coolant channel assist to develop the countermeasure for avoiding hot spot development in a gas turbine rotor blade.

8. Conclusions and Recommendations

This review summarizes and compares recent findings regarding rotating channels with cooling applications in gas turbine rotor blades [1–103]. The impingement flow and swirl chamber were mostly utilized for leading-edge cooling. The multi-pass channel with ribs and dimples is commonly deployed along the internal coolant channel over the mid-chord region. Considering the requirement for structural enforcement and the geometrical limitation at the tail end of a gas turbine rotor blade, cooling performances are mostly boosted by a variety of pin fins and newly emerged latticework in narrow rectangular or

trapezoidal channels. While the typical rotational effects characterized by Re , Ro , and Bu on the cooling performances of these rotating channels are basically followed, the geometrical complexities, coolant flow supplements, and various flow entry/exit and thermal boundary conditions differentiate their aerothermal performances to large extents. The following salient points emerge from the current review for future studies with a strategic aim to avoid hot spot development in a gas turbine rotor blade.

1. The novelty in experimental method for acquiring the heat transfer data at the realistic Bu range of approximately 4.95–17.85 with a density ratio above 1.1 should be prioritized for emulating the realistic buoyancy effect on the heat transfer performance in an internal coolant channel of a gas turbine rotor blade.
2. The data analysis and presentation in terms of $(\eta_w - \eta_f)$ assist to visualize the combined effects of spatial Nu variation and raised downstream fluid temperatures, especially for the multi-pass coolant channel with a long heating path.
3. The HTE benefits from the positive utilization of the Coriolis force effect by arranging the coolant walls in contact with the hot gas to be the destabilized sides of the internal cooling channels were experimentally affirmed [39,40]. The novel interconnected channels with radial inflow and outflow under this cooling framework is worthy of future exploration.
4. Along with the continuing endeavors aimed at promoting the aerothermal performances of the rotating coolant passages, the direct mixing of cold and hot flow streams using the supplementary coolant supply or the internal effusion exhibit considerable HTE improvements due to the reduction in local fluid temperatures and the relevant HTE flow mechanisms.
5. The identification of the minimum heat transfer scenario aimed at determining the critical Ro and Bu for a particular cooling flow configuration is advantageous for a designer to determine the effective diameter of a rotating coolant channel for operating a cooling network away from the worst rotational conditions.
6. The full Nu maps involving Re , Ro , and Bu effects for a rotating coolant channel in realistic engine conditions are necessary to reveal Nu levels at the locations with the local minimum heat transfer rates in a rotating channel to assist the formulation of the countermeasures for avoiding hot spot development in a gas turbine rotor blade.

Author Contributions: Conceptualization, S.W.C. and P.-S.W.; methodology, S.W.C. and P.-S.W.; investigation, T.-Y.W. and W.-L.C.; resources, S.W.C.; data curation, T.-Y.W. and W.-L.C.; writing—original draft preparation, S.W.C.; writing—review and editing, S.W.C.; supervision, S.W.C. and P.-S.W.; project administration, S.W.C.; funding acquisition, S.W.C. All authors have read and agreed to the published version of the manuscript.

Funding: This research was funded by Ministry of Science and Technology, Taiwan, under the grant number MOST 111-2221-E-006-086-MY3.

Data Availability Statement: No new data were created or analyzed in this study. Data sharing is not applicable to this article.

Conflicts of Interest: The authors declare no conflict of interest.

Nomenclature

English symbols

Bu	rotating buoyancy number = $Ro^2 \beta (T - T_{ref}) \epsilon$
d_h	channel hydraulic diameter (m)
h	convective heat transfer coefficient ($W m^{-2} K^{-1}$)
k_f	thermal conductivity of fluid ($W m^{-1} K^{-1}$)
Nu	Nusselt number = $h d_h / k_f$
P	static pressure involving hydrostatic effect of centrifugal force (Pa)
P'	dimensionless pressure = $P^* / (\rho_{ref} W_m^2)$
R	gas constant of coolant ($J kg^{-1} K^{-1}$)

R_m	mean radius of rotating channel (m)
Re	Reynolds number = $\rho_{ref} W_m d_h / \mu$
T	local fluid temperature (K)
T_{ref}	referenced fluid temperature (K)
U	dimensionless fluid velocity in x direction = u / W_m
V	dimensionless fluid velocity in y direction = v / W_m
\vec{V}^*	dimensionless fluid velocity vector = \vec{V} / W_m
W	dimensionless fluid velocity in z direction = w / W_m
W_m	mean fluid velocity in z direction (ms^{-1})
X^*	dimensionless x coordinate = x / d_h
Y^*	dimensionless y coordinate = y / d_h
Z^*	dimensionless z coordinate = z / d_h
Greek symbols	
β	thermal expansion coefficient of fluid = $1/T$ (K^{-1})
ε	eccentricity ratio = H/d_h or R/d_h
μ	fluid viscosity ($\text{kgm}^{-1}\text{s}^{-1}$)
ω	dimensionless angular velocity vector = $\vec{\omega} / \Omega$
ρ_{ref}	fluid density at T_{ref} (kgm^{-3})
Suffix	
0	static (non-rotating) channel
∞	fully developed flow in straight smooth-walled plain tube

References

- Morris, W.D. A rotating facility to study heat transfer in the cooling passages of turbine rotor blades. *Proc. Inst. Mech. Eng. Part A J. Power Energy* **1996**, *210*, 55–63. [\[CrossRef\]](#)
- Chang, S.W.; Morris, W.D. Heat transfer in a radially rotating square duct fitted with in-line transverse. *Int. J. Therm. Sci. Ribs* **2003**, *42*, 267–282. [\[CrossRef\]](#)
- Wagner, J.H.; Johnson, B.V.; Kopper, F.C. Heat transfer in rotating serpentine passages with smooth walls. *Trans. ASME J. Turbomach.* **1991**, *113*, 321–330. [\[CrossRef\]](#)
- Wagner, J.H.; Johnson, B.V.; Graziani, R.A.; Yeh, F.C. Heat transfer in rotating serpentine passages with trips normal to the flow. *Trans. ASME J. Turbomach.* **1992**, *114*, 847–857. [\[CrossRef\]](#)
- Johnson, B.V.; Wagner, J.H.; Steuber, G.D.; Yeh, F.C. Heat transfer in rotating serpentine passages with trips skewed to the flow. *Trans. ASME J. Turbomach.* **1994**, *116*, 113–123. [\[CrossRef\]](#)
- Chang, S.W.; Liou, T.-M.; Po, Y. Coriolis and rotating buoyancy effect on detailed heat transfer distributions in a two-pass square channel roughened by 45° ribs at high rotation numbers. *Int. J. Heat Mass Transf.* **2010**, *53*, 1349–1363. [\[CrossRef\]](#)
- Morris, W.D.; Chang, S.W. Heat transfer in a radially rotating smooth-walled tube. *Aeronaut. J.* **1998**, *102*, 277–285.
- Du, W.; Luo, L.; Jiao, Y.; Wang, S.; Li, X.; Bengt, S. Heat transfer in the trailing region of gas turbines—A state-of-the-art review. *Appl. Therm. Eng.* **2021**, *199*, 117614. [\[CrossRef\]](#)
- Giugno, A.; Sorce, A.; Cuneo, A.; Barberis, S. Effects of market and climatic conditions over a gas turbine combined cycle integrated with a heat pump for inlet cooling. *Appl. Energy* **2021**, *290*, 116724. [\[CrossRef\]](#)
- Han, J.-C.; Wright, L.M. Enhanced Internal Cooling of Turbine Blades and Vanes. In *The Gas Turbine Handbook*; U.S. DOE, National Energy Technology Laboratory: Morgantown, WV, USA, 2007; pp. 321–352.
- Chang, S.W.; Chiang, P.-A.; Cai, W.L. Thermal performance of impinging jet-row onto trapezoidal channel with different effusion and discharge conditions. *Int. J. Therm. Sci.* **2021**, *159*, 106590. [\[CrossRef\]](#)
- Chang, S.W.; Yu, K.-C. Thermal performance of radially rotating trapezoidal channel with impinging jet-row. *Int. J. Heat Mass Transf.* **2019**, *136*, 246–264. [\[CrossRef\]](#)
- Amagasa, S.; Shimomura, K.; Kadowaki, M.; Takeishi, K.; Kawai, H. Study on the turbine vane and blade from a 1500°C class industrial gas turbine. *Trans. ASME J. Eng. Gas Turbine Power* **1994**, *116*, 591–604.
- Chang, S.W.; Huang, S.-W. Aerothermal performance of a rotating two-pass furrowed channel roughened by angled ribs. *Appl. Therm. Eng.* **2021**, *199*, 117613. [\[CrossRef\]](#)
- Cai, L.; He, Y.; Wang, S.; Li, Y.; Li, F. Thermal-fluid-solid coupling analysis on the temperature and thermal stress field of a nickel-base superalloy turbine blade. *Materials* **2021**, *14*, 3315. [\[CrossRef\]](#) [\[PubMed\]](#)
- Chang, S.W.; Yang, T.L.; Huang, C.C.; Chiang, K.F. Endwall heat transfer and pressure drop in rectangular channels with attached and detached circular pin-fin array. *Int. J. Heat Mass Transf.* **2008**, *51*, 5247–5259. [\[CrossRef\]](#)
- Ames, F.E.; Dvorak, L.A. Turbulent transport in pin fin arrays: Experimental data and predictions. *ASME Trans. J. Turbomach.* **2006**, *128*, 71–81. [\[CrossRef\]](#)

18. Chyu, M.K.; Hsing, Y.C.; Shih, T.P.; Natarajan, V. Heat transfer contributions of pins and endwall in pin-fin arrays: Effects of thermal boundary condition modeling. *ASME Trans. J. Turbomach.* **1999**, *121*, 257–263. [\[CrossRef\]](#)
19. Chang, S.W.; Hu, Y.-W. Endwall thermal performances of radially rotating rectangular channel with pin-fins on skewed rib lands. *Int. J. Heat Mass Transf.* **2014**, *69*, 173–190. [\[CrossRef\]](#)
20. Rao, Y.; Wan, C.; Xu, Y. An experimental study of pressure loss and heat transfer in the d channels with various dimple depths. *Int. J. Heat Mass Transf.* **2012**, *55*, 6723–6733. [\[CrossRef\]](#)
21. Han, J.C.; Zhang, Y.M.; Lee, C.P. Augmented heat transfer in square channel with parallel crossed and V-shaped angled ribs. *ASME Trans. J. Turbomach.* **1991**, *113*, 590–597. [\[CrossRef\]](#)
22. Jeng, T.M. Thermal performance of in-line diamond-shaped pin-fins in a rectangular duct. *Int. Commun. Heat Mass Transf.* **2006**, *33*, 1139–1146. [\[CrossRef\]](#)
23. Chyu, M.K.; Yen, C.H.; Siw, S. Comparison of heat transfer from staggered pin fin arrays with circular, cubic and diamond shaped elements. *Turbo Expo Power Land Sea Air.* **2007**, 47934, 991–999.
24. Wright, L.M.; Lee, E.; Han, J.C. Effect of rotation on heat transfer in rectangular channels with pin-fins. *AIAA J. Thermophys. Heat Transf.* **2004**, *18*, 263–272. [\[CrossRef\]](#)
25. Elyyan, M.A.; Tafti, D.K. Investigation of Coriolis forces effect of flow structure and heat transfer distribution in a rotating dimpled channel. *ASME Trans. J. Turbomach.* **2012**, *134*, 031007. [\[CrossRef\]](#)
26. Hsieh, S.S.; Tsai, H.-H.; Chan, S.-C. Local heat transfer in rotating square-rib-roughened and smooth channels with jet impingement. *Int. J. Heat Mass Transf.* **2004**, *47*, 2769–2784. [\[CrossRef\]](#)
27. Adreini, A.; Brberri, E.; Cocchi, L.; Facchini, B.; Massini, D.; Pievaroli, M. Heat transfer investigation on an internal cooling system of a gas turbine leading edge model. *Energy Procedia* **2015**, *82*, 222–229. [\[CrossRef\]](#)
28. Cocchi, L.; Facchini, B.; Picchi, A. Heat transfer measurements in leading-edge cooling geometry under rotating conditions. *J. Thermophys. Heat Transf.* **2019**, *33*, 844–855. [\[CrossRef\]](#)
29. Furlani, L.; Armellini, A.; Casarsa, L. Rotational effects on the flow field inside a leading edge impingement cooling passage. *Exp. Therm. Fluid Sci.* **2016**, *76*, 57–66. [\[CrossRef\]](#)
30. Elston, C.A.; Wright, L.M. Leading edge jet impingement under high rotation numbers. *ASME Trans. J. Therm. Sci. Eng. Appl.* **2017**, *9*, 021010. [\[CrossRef\]](#)
31. Singh, P.; Ekkad, S.V. Detailed heat transfer measurements of jet impingement on dimpled target surface under rotation. *ASME Trans. J. Therm. Sci. Eng. Appl.* **2018**, *10*, 031006. [\[CrossRef\]](#)
32. Wang, J.; Deng, H.; Tao, Z.; Li, Y.; Zhu, J. Heat transfer in a rotating rectangular channel with impingement jet and film holes. *Int. J. Therm. Sci.* **2021**, *163*, 106832. [\[CrossRef\]](#)
33. Deng, H.; Wang, Z.; Wang, J.; Li, H. Flow and heat transfer in a rotating channel with impingement cooling and film extraction. *Int. J. Heat Mass Transf.* **2021**, *180*, 121751. [\[CrossRef\]](#)
34. Li, H.; Deng, H.; Qiu, L. Effect of channel orientation on heat transfer in a rotating impingement cooling channel. *Int. J. Heat Mass Transf.* **2022**, *187*, 122493. [\[CrossRef\]](#)
35. Gleze, B.; Moon, H.K.; Kerrebrock, J.; Bons, J.; Guenette, G. Heat transfer in a rotating radial channel with swirling internal flow. *Int. Gas Turbine Aeroengine Congr. Exhib.* **1998**, 98-GT-214, 1–7.
36. Rao, Y.; Biegger, C.; Weigand, B. Heat transfer and pressure loss in swirl tubes with one and multiple tangential jets pertinent to gas turbine internal cooling. *Int. J. Heat Mass Transf.* **2017**, *106*, 1356–1367. [\[CrossRef\]](#)
37. Wang, J.; Liu, J.; Wang, L.; Sundén, B.; Wang, S. Conjugated heat transfer investigation with racetrack-shaped jet hole and double swirling chamber in rotating jet impingement. *Numer. Heat Transf. Part A Appl.* **2018**, *73*, 768–787. [\[CrossRef\]](#)
38. Tansakul, P.; Thawornsathit, P.; Juntasaro, V.; Juntasaro, E. Buoyancy effect on leading edge cooling of a rotating turbine blade. *Trans. ASME J. Therm. Sci. Eng. Appl.* **2022**, *14*, 111015. [\[CrossRef\]](#)
39. Chang, S.W.; Yang, T.L.; Wang, W.J. Heat transfer in a rotating twin-pass trapezoidal-sectioned passage roughened by skewed ribs on two opposite walls. *J. Heat Transf. Eng.* **2006**, *27*, 63–79. [\[CrossRef\]](#)
40. Guo, X.; Xu, H.; Li, X.; Ren, J. Flow and heat transfer characteristics of Coriolis-utilization rotating rectangular smooth cooling U-channel. *Appl. Therm. Eng.* **2022**, *211*, 118420.
41. Su, G.; Chen, H.-C.; Han, J.-C.; Heidmann, J.D. Computation of flow and heat transfer in rotating two-pass rectangular channels ($AR = 1:1$, $1:2$, and $1:4$) with smooth wall by a Reynolds stress turbulence model. *Int. J. Heat Mass Transf.* **2004**, *47*, 5665–5683. [\[CrossRef\]](#)
42. Liou, T.-M.; Chang, S.W.; Chen, J.S.; Yang, T.L.; Lan, Y.-A. Influence of channel aspect ratio on heat transfer in rotating rectangular ducts with skewed ribs at high rotation numbers. *Int. J. Heat. Mass Transf.* **2009**, *52*, 5309–5322. [\[CrossRef\]](#)
43. Murata, A.; Mochizuki, S. Large eddy simulation with a dynamic subgrid-scale model of turbulent heat transfer in an orthogonally rotating rectangular duct with transverse rib turbulators. *Int. J. Heat Mass Transf.* **2000**, *43*, 1243–1259. [\[CrossRef\]](#)
44. Murata, A.; Mochizuki, S. Effect of cross-sectioned aspect ratio on turbulent heat transfer in an orthogonally rotating rectangular duct with angled rib turbulators. *Int. J. Heat Mass Transf.* **2003**, *46*, 3119–3133. [\[CrossRef\]](#)
45. Kim, K.M.; Kim, Y.Y.; Lee, D.H.; Rhee, D.H.; Cho, H.H. Influence of duct aspect ratio on heat/mass transfer in coolant passages with rotation. *Int. J. Heat Fluid Flow* **2007**, *28*, 357–373. [\[CrossRef\]](#)

46. Chang, S.W.; Lees, A.W.; Liou, T.-M.; Hong, G.F. Heat transfer of a radially rotating furrowed channel with two opposite skewed sinusoidal wavy walls. *Int. J. Therm. Sci.* **2010**, *49*, 769–785. [\[CrossRef\]](#)
47. Mayo, I.; Arts, T.; El-Habib, A.; Parres, B. Two-dimensional heat transfer distribution of a rotating ribbed channel at different Reynolds numbers. *ASME Trans. J. Turbomach.* **2015**, *137*, 031002. [\[CrossRef\]](#)
48. Xu, G.; Li, Y.; Deng, H. Effect of rib spacing on heat transfer and friction in a rotating two-pass square channel with asymmetrical 90-deg rib turbulators. *Appl. Therm. Eng.* **2015**, *80*, 386–395. [\[CrossRef\]](#)
49. Wang, Z.; Corral, R. Effect of uneven wall heating conditions under different buoyancy numbers for a one side rib-roughened rotating channel. *ASME Trans. J. Turbomach.* **2017**, *139*, 111011. [\[CrossRef\]](#)
50. Deng, H.; Li, Y.; Tao, Z.; Xu, G.; Tian, S. Pressure drop and heat transfer performance in a rotating two-pass channel with staggered 45-deg ribs. *Int. J. Heat Mass Transf.* **2017**, *108*, 2273–2282. [\[CrossRef\]](#)
51. Singh, P.; Li, W.; Ekkad, S.V.; Ren, J. A new cooling design for rib roughened two-pass channel having positive effects of rotation on heat transfer enhancement on both pressure and suction side internal walls of a gas turbine blade. *Int. J. Heat Mass Transf.* **2017**, *115*, 6–20. [\[CrossRef\]](#)
52. Wang, J.; Liu, J.; Wang, L.; Sunden, B.; Wang, S. Numerical investigation of heat transfer and fluid flow in a rotating rectangular channel with variously discrete ribs. *Appl. Therm. Eng.* **2018**, *129*, 1369–1381. [\[CrossRef\]](#)
53. Yan, H.; Luo, L.; Sun, P.; Du, W.; Wang, S.; Huang, D. Combined effects of bleed hole extraction and rotation on internal heat transfer in a ribbed two-pass channel. *Int. Commun. Heat Mass Transf.* **2022**, *133*, 105964. [\[CrossRef\]](#)
54. Li, H.-L.; Chiang, H.-W.D.; Hsu, C.N. Jet impingement and forced convection cooling experimental study in rotating turbine blades. *Int. J. Turbo Jet Engines* **2011**, *28*, 147–158. [\[CrossRef\]](#)
55. Kim, S.; Choi, E.Y.; Kwak, J.S. Effect of channel orientation on the heat transfer coefficient in the smooth and dimpled rotating rectangular channels. *ASME Trans. J. Heat Transf.* **2012**, *134*, 064504. [\[CrossRef\]](#)
56. Lamont, J.A.; Ekkad, S.V.; Alvin, M.A. Effects of rotation on heat transfer for a single row jet impingement array with crossflow. *ASME Trans. J. Heat Transf.* **2012**, *134*, 082202. [\[CrossRef\]](#)
57. Chang, S.W.; Liou, T.-M.; Chen, W.-C. Influence of radial rotation on heat transfer in a rectangular channel with two opposite walls roughened by hemispherical protrusions at high rotation numbers. *ASME Trans. J. Turbomach.* **2012**, *134*, 011010. [\[CrossRef\]](#)
58. Xu, G.; Chen, Y.; Wen, J. Heat transfer in a rotating rectangular channel (AR=4) with dimples and sidewall bleeds. *Int. J. Heat Mass Transf.* **2020**, *150*, 119118. [\[CrossRef\]](#)
59. Chang, S.W.; Wu, P.-S.; Chen, C.-S.; Weng, C.-C.; Jiang, Y.-R.; Shihe, S.-H. Thermal performance of radially rotating two-pass S-shaped zig-zag channel. *Int. J. Heat Mass Transf.* **2017**, *115*, 1011–1031. [\[CrossRef\]](#)
60. Siw, S.C.; Chyu, M.K.; Alvin, M.A. Heat transfer and pressure loss characteristics of zig-zag channel with rib-turbulators. *ASME Turbo Expo* **2013**, GT2013-95407, 1–10.
61. Dutta, S.; Han, J.C.; Lee, C.P. Local heat transfer in a rotating two-pass ribbed triangular duct with two model orientations. *Int. J. Heat Mass Transf.* **1996**, *39*, 707–715. [\[CrossRef\]](#)
62. Chang, S.W.; Liou, T.-M.; Lee, T.-H. Thermal performance comparison between radially rotating ribbed parallelogram channels with and without dimples. *Int. J. Heat Mass Transf.* **2012**, *55*, 3541–3559. [\[CrossRef\]](#)
63. Liou, T.-M.; Chang, S.W.; Yang, C.-C. Heat transfer and pressure drop measurements of rotating twin-pass parallelogram ribbed channel. *Int. J. Therm. Sci.* **2014**, *79*, 206–219. [\[CrossRef\]](#)
64. Liou, T.-M.; Chang, S.W.; Lan, Y.-A.; Chan, S.-P. Isolated and coupled effects of rotating and buoyancy number on heat transfer and pressure drop in a rotating two-pass parallelogram channel with transverse ribs. *ASME Trans. J. Heat Transf.* **2018**, *140*, 032001. [\[CrossRef\]](#)
65. Brahim, B.; Miloud, A. Numerical simulation of the effect of channel orientation on fluid flow and heat transfer at high buoyancy number in a rotating two-pass channel with angled ribs. *ASME Trans. J. Heat Transf.* **2019**, *141*, 022502. [\[CrossRef\]](#)
66. Li, H.; You, R.; Deng, H.; Tao, Z.; Zhu, J. Heat transfer investigation in a rotating U-turn smooth channel with irregular cross-section. *Int. J. Heat Mass Transf.* **2016**, *96*, 267–277. [\[CrossRef\]](#)
67. Tao, Z.; Yang, M.; Deng, H.; Li, H.; Tian, S. Heat transfer study in a rotating ribbed two-pass channel with engine-similar cross section at high rotation number. *Appl. Therm. Eng.* **2016**, *106*, 681–696. [\[CrossRef\]](#)
68. Chen, A.F.; Wu, H.-W.; Wang, N.; Han, J.-C. Heat transfer in a rotating cooling channel (AR = 2:1) with rib turbulators and a tip turning vane. *ASME Trans. J. Heat Transf.* **2018**, *140*, 102007. [\[CrossRef\]](#)
69. Chen, A.F.; Shiau, C.-C.; Han, J.-C.; Krewinkel, R. Heat transfer in a rotating two-pass rectangular channel featuring reduced cross-sectional area after tip turn (aspect ratio = 4:1 to 2:1) with profiled 60 deg angled ribs. *ASME Trans. J. Turbomach.* **2019**, *141*, 071008. [\[CrossRef\]](#)
70. Sahin, I.; Chen, A.F.; Shiau, C.-C.; Han, J.-C.; Krewinkel, R. Effect of 45-deg rib orientations on heat transfer in a rotating two-pass channel with aspect ratio from 4:1 to 2:1. *ASME Trans. J. Turbomach.* **2020**, *142*, 071003. [\[CrossRef\]](#)
71. Chen, I.-L.; Sahin, I.; Wright, L.M.; Han, J.-C.; Krewinkel, R. Heat transfer in a rotating, two-pass, variable aspect ratio cooling channel with profiled V-shaped ribs. *ASME Trans. J. Turbomach.* **2021**, *143*, 081013. [\[CrossRef\]](#)
72. Parsons, J.A.; Han, J.-C.; Zhang, Y. Wall heating effect on local heat transfer in a rotating two-pass square channel with 90° rib turbulators. *Int. J. Heat Mass Transf.* **1996**, *37*, 1411–1420. [\[CrossRef\]](#)

73. Abdel-Wahab, S.; Tafti, D.K. Large eddy simulation of flow and heat transfer in a 90 deg ribbed duct with rotation: Effect of Coriolis and centrifugal buoyancy forces. *ASME Trans. J. Turbomach.* **2004**, *126*, 627–636. [\[CrossRef\]](#)
74. Kim, K.M.; Lee, D.H.; Cho, H.H. Detailed measurement of heat/mass transfer and pressure drop in a rotating two-pass duct with transverse ribs. *Heat Mass Transf.* **2007**, *43*, 801–815. [\[CrossRef\]](#)
75. Sleiti, A.K.; Kapat, J.S. Effect of Coriolis and centrifugal forces on turbulence and transport at high rotation and density ratios in a rib-roughened channel. *Int. J. Therm. Sci.* **2008**, *47*, 609–619. [\[CrossRef\]](#)
76. Saha, A.K.; Acharya, S. Turbulent heat transfer in ribbed coolant passages of different aspect ratios: Parametric effects. *Int. J. Heat Mass Transf.* **2006**, *129*, 449–463. [\[CrossRef\]](#)
77. Morris, W.D.; Farhadi, R.-A.K. Convective heat transfer in rotating ribbed tubes. *Int. J. Heat Mass Transf.* **1996**, *39*, 2253–2266. [\[CrossRef\]](#)
78. Chang, S.W.; Liou, T.-M.; Chiou, S.F.; Chang, S.F. Heat transfer in high-speed rotating trapezoidal duct with rib-roughened surfaces and air bleeds from the wall on apical side. *Int. J. Heat Mass Transf.* **2008**, *130*, 061702. [\[CrossRef\]](#)
79. Lee, D.H.; Rhee, D.H.; Kim, K.M.; Cho, H.H.; Moon, H.K. Heat transfer and flow temperature measurements in a rotating triangular channel with various rib arrangements. *Heat Mass Transf.* **2009**, *45*, 1543–1553. [\[CrossRef\]](#)
80. Chang, S.W.; Liou, T.-M.; Lee, T.H. Thermal performance of developing flow in a radially rotating parallelogram channel with 45° ribs. *Int. J. Therm. Sci.* **2012**, *52*, 186–204. [\[CrossRef\]](#)
81. Wright, L.M.; Liu, Y.-H.; Han, J.-C.; Chopra, S. Heat transfer in trailing edge, wedge-shaped cooling channels under high rotation numbers. *ASME Trans. J. Heat Transf.* **2008**, *130*, 071701. [\[CrossRef\]](#)
82. Li, Y.; Deng, H.; Tao, Z.; Xu, G.; Chen, Y. Heat transfer characteristics in a rotating trailing edge internal cooling channel with two coolant inlets. *Int. J. Heat Mass Transf.* **2017**, *105*, 220–229. [\[CrossRef\]](#)
83. Deng, H.; Chen, Y.; Tao, Z.; Li, Y.; Qiu, L. Heat transfer in a two-inlet rotating rectangular channel with side-wall fluid extraction. *Int. J. Heat Mass Transf.* **2017**, *105*, 525–534. [\[CrossRef\]](#)
84. Deng, H.; Cheng, Y.; Li, Y.; Li, B.; Qiu, L. Heat transfer in a two-inlet rotating wedge-shaped channel with various locations of the second inlet. *Int. J. Heat Mass Transf.* **2017**, *106*, 25–34. [\[CrossRef\]](#)
85. Deng, H.; Li, L.; Zhu, J.; Tao, Z.; Tian, S.; Yang, Z. Heat transfer of a rotating two-inlet trailing edge channel with lateral fluid extractions. *Int. J. Therm. Sci.* **2018**, *125*, 313–323. [\[CrossRef\]](#)
86. Chang, S.W.; Liou, T.-M.; Yang, T.L.; Hong, G.F. Heat transfer in radially rotating pin-fin channel at high rotation numbers. *ASME Trans. J. Turbomach.* **2010**, *132*, 021019. [\[CrossRef\]](#)
87. Park, J.S.; Kim, K.M.; Lee, D.H.; Cho, H.H.; Chyu, M. Heat transfer in rotating channel with inclined pin-fins. *ASME Trans. J. Turbomach.* **2011**, *133*, 021003. [\[CrossRef\]](#)
88. Chang, S.W.; Liou, T.-M.; Lee, T.-H. Heat transfer of a rotating rectangular channel with a diamond-shaped pin-fin array at high rotation numbers. *ASME Trans. Turbomach.* **2013**, *135*, 041007. [\[CrossRef\]](#)
89. Huang, S.-C.; Wang, C.-C.; Liu, Y.-H. Heat transfer measurement in a rotating cooling channel with staggered and inlined pin-fin array using liquid crystal and stroboscopy. *Int. J. Heat Mass Transf.* **2017**, *115*, 364–376. [\[CrossRef\]](#)
90. Huang, S.C.; Wang, C.-C.; Liu, Y.-H. Channel orientation effect on endwall heat transfer in rotating passages with pin-fins. *Int. J. Heat Mass Transf.* **2019**, *136*, 1115–1126. [\[CrossRef\]](#)
91. Hung, S.-C.; Huang, S.-C.; Liu, Y.-H. Effect of nonuniform pin size on heat transfer in a rotating rectangular channel with pin-fin arrays. *Appl. Therm. Eng.* **2019**, *163*, 114393. [\[CrossRef\]](#)
92. Du, W.; Luo, L.; Wang, S.; Zhang, X. Effect of the dimple location and rotating number on the heat transfer and flow structure in a pin finned channel. *Int. J. Heat Mass Transf.* **2018**, *127*, 111–129. [\[CrossRef\]](#)
93. Luo, L.; Yan, H.; Yang, S.; Du, W.; Wang, S.; Sunden, B.; Zhang, X. Convergence angle and dimple shape effects on the heat transfer characteristics in a rotating dimple-pin fin wedge duct. *Numer. Heat Transf. Part A* **2018**, *74*, 1611–1635. [\[CrossRef\]](#)
94. Li, H.; Deng, H.; Bai, L.; Zhu, J.; Tian, S.; Qiu, L. Heat transfer in a rotating two-inlet wedge-shaped channel with pin-fins. *Int. J. Heat Mass Transf.* **2020**, *163*, 120380. [\[CrossRef\]](#)
95. Liang, C.; Rao, Y. Numerical study of turbulent flow and heat transfer in channels with detached pin fin arrays under stationary and rotating conditions. *Int. J. Therm. Sci.* **2021**, *160*, 106659. [\[CrossRef\]](#)
96. Yan, H.; Luo, L.; Zhang, J.; Du, W.; Wang, S.; Huang, D. Flow structure and heat transfer characteristics of a pin-finned channel with upright/curved/inclined pin fins under stationary and rotating conditions. *Int. Commun. Heat Mass Transf.* **2021**, *127*, 105483. [\[CrossRef\]](#)
97. Madhavan, S.; Singh, P.; Ekkad, S. Effect of rotation on heat transfer in AR = 2:1 and AR = 4:1 channels connected by a series of crossover jets. *ASME Trans. J. Turbomach.* **2022**, *144*, 061011. [\[CrossRef\]](#)
98. Liang, C.; Rao, Y.; Chen, J.; Zhang, P. Experimental and numerical study of the turbulent flow and heat transfer in a wedge-shaped channel with guiding pin fin arrays under rotating conditions. *ASME Trans. J. Turbomach.* **2022**, *144*, 071007. [\[CrossRef\]](#)
99. Zhang, X.; Li, H.; Tian, Y.; You, R.; Zhang, D.; Wu, A. Heat transfer in a rotating lateral outflow trapezoidal channel with pin fins under high rotation numbers and Reynolds numbers. *Appl. Therm. Eng.* **2022**, *213*, 118725. [\[CrossRef\]](#)
100. Jing, Q.; Xie, Y.; Zhang, D. Numerical investigation of flow and heat transfer in rotating trapezoidal channel with lateral slots and dimple structure. *Int. Commun. Heat Mass Transf.* **2020**, *118*, 104865. [\[CrossRef\]](#)

101. Chen, Y.; Xu, G.; Wen, J.; Zhu, C. Rotational heat transfer in a rectangular cooling channel with compound turbulators of pin-fins and dimples. *Int. J. Heat Mass Transf.* **2022**, *184*, 121897. [[CrossRef](#)]
102. Oh, I.T.; Kim, K.M.; Lee, D.H.; Park, J.S.; Cho, H.H. Local heat/mass transfer and friction loss measurement in a rotating matrix cooling channel. *ASME Trans. J. Heat Transf.* **2012**, *134*, 011901.
103. Du, W.; Luo, L.; Wang, S.; Liu, J.; Sunden, B. Effect of the broken rib locations on the heat transfer and fluid flow in a rotating latticework duct. *ASME Trans. J. Heat Transf.* **2019**, *141*, 102102. [[CrossRef](#)]
104. Chang, S.W.; Hsu, C.J. Effect of internal effusion on aerothermal performance of a three-pass channel roughened by angled ribs and pin-fins with lateral flow exit. *Int. J. Heat Mass Transf.* **2022**, *198*, 123387. [[CrossRef](#)]

Disclaimer/Publisher's Note: The statements, opinions and data contained in all publications are solely those of the individual author(s) and contributor(s) and not of MDPI and/or the editor(s). MDPI and/or the editor(s) disclaim responsibility for any injury to people or property resulting from any ideas, methods, instructions or products referred to in the content.